PAPER

Check for updates

LSNR:GO template for BSA interaction, photo and sonocatalytic reductions of fluorescent dyes in aqueous solutions†

Krishan Kumar, Bhargab Sahoo, Tara Chand Meghwal and Man Singh [ID] *

Lanthanide sulfide nanorods (LSNRs) were synthesized by fusing sodium (Na) metal with hexahydrate chloride salts of lanthanum (La), cerium (Ce), terbium (Tb), and holmium (Ho) ($LnCl_3·6H_2O$) with $4f^0$, $4f^1$, $4f^9$, and $4f^{11}$ electrons ($4f^{\#e}$), respectively. Na reduced $LnCl_3·6H_2O$ to $Ln(OH)_3 + 3H_2$ as a crash reaction methodology (CRM). Aq-$Ln(OH)_3$ with H_2S developed La_2S_3, Ce_2S_3, Tb_2S_3, Ho_2S_3, LSNRs, which were doped with graphene oxide (GO) at ~60 for an LSNR:GO template (LGT), characterized with XRD, FT-IR, TGA/DTG, SEM, DLS, FESEM + EDS, C, H, N/S elemental analysis, Raman spectroscopy and survismetry. The 0.010 g% aq-LSNR and LGT were studied separately and with 0.010 g% (w/v) bovine serum albumin (BSA) from 283.15 to 315.15 K, and 0.002−0.010 g% @0.004 g% LSNR and LGT with 0.010% aq-BSA at 298.15 K. Their densities (ρ, g cm^{-3}), viscosity (η, mPa s), sound velocity (μ, m s^{-1}), surface tension (γ, mN m^{-1}), friccohesity (σ, s cm^{-1}), isentropic compressibility ($K_{s,\phi}$, cm^2 g^{-1}), activation energy (E_a, J mol^{-1}), and the thermodynamic parameters enthalpy (ΔH, kJ mol^{-1}), Gibbs free energy (ΔG, kJ mol^{-1}), and entropy (ΔS, J mol^{-1}) imply interactive activities with globular protein. LSNRs and LGT photocatalytically (PCR) and sonocatalytically (SCR) reduced methylene blue (MB), brilliant blue red (BBR), brilliant blue green (BBG) and methyl orange (MO). LGT recycled wastewater containing fluorescent dyes in ~60 min while GO did it in 120 min and LSNRs in 24 h under sunlight (SL). Sonicated dyes with aq-LGT at 28 kHz for 5, 10, 20, 30, 60 min were reduced with 40−90% Φ compared to 98% with PCR in 1st order kinetics. The physicochemical properties (PCPs) of LSNR and LGT predicted their structural activities with reusability.

1. Introduction

Lanthanide and GO individually have been widely used for research and industrial applications, but their interfaces have not yet been reported.[1,2] Therefore, developing their LGT has been a novel research project and it was found to be relentlessly stable, reusable, and efficient photocatalyst to split water expeditiously compared to GO and LSNRs alone.[3,4] Synthesizing new photocatalyzing nanomaterials for reducing wastewater effluents in sunlight is a biological and natural requirement for recycling. PCR splits wastewater into H_2 and O_2 gases, and also recycles its fluorescent effluents and transitional metals to collect usable water.[5] For decades, the focus has been on developing photocatalyzing metallic organic frameworks, metallic biocomplexes, and bimetallic complexes using transitional metals,

as reported in previous studies.[5,6] Transition metals are comparatively easy to handle, and their crystalline water molecules are removed at NTP unlike the 800–1300 for lanthanide metals that hinders chemical processes.[7] The crystalline $6H_2O$ of $LnCl_3·6H_2O$ is not detached by dissolving it in water at NTP, though, its Cl^- dissociate and respond to $AgNO_3$ but are unable to form Ln_2S_3. As a result, researchers have been heating $LnCl_3·6H_2O$ up to 800–1300 to prepare Ln_2S_3 without understanding the contraction effect of $4f^{\#}$ electrons[8,9] (Table 1). The 6s electrons shield a nuclear charge that affects the activities of $4f^{\#e}$ and the water dipoles are strongly bound with the nuclear charge, restricting lanthanides interacting with H_2S for LSNR preparation and applications in the areas of photocatalysts, and adsorbents. The problem of preparing Ln_2S_3 by heating to detach a crystalline $6H_2O$ from $LnCl_3·6H_2O$ due to the energy barrier for electronic reduction of $6H_2O$ is resolved by allowing a reaction with sodium metal at 50 with $LnCl_3·6H_2O$. The $3s^1$ electron of sodium metal reduces $6H_2O$ to H_2 and $Ln(OH)_3$ (Fig. 3). The idea of synthesizing LSNRs and LGT for use as photocatalysts and adsorbents has never been initiated, despite huge industrial potential in areas of effluent disposal of

School of Chemical Sciences, Central University of Gujarat, Sector-30(382030), Gandhinagar, India. E-mail: Mansingh50@hotmail.com, Krishan8053649040@gmail.com, rajatvlrc@gmail.com, tarachandmeghwal9660@gmail.com

† Electronic supplementary information (ESI) available. See DOI: https://doi.org/10.1039/d2ya00274d

Table 1 Comparative study of lanthanide sulfide preparation with temperature

Sr. no.	Temp. (°C)	Method	Ref.
This study	50–60	Crash reaction methodology	
1	800–1000	Hydrothermal process	26 and 32
2	650–750	Solid phase reaction	8 and 33
3	500–650	Solvothermal	34 and 35
4	100–500	Hydrothermal reaction	21 and 36
5	500–1000	Solvothermal	37 and 38

infectious and hazardous biomedicals, and also, for solving the most tedious and hazardous chemical processes. LSNRs and LGT act as renewable energy storage systems and dopants with pharmaceuticals, digital inks, textiles, integrated circuits (ICs), and heat sensors.[5,6,10,11] PCPs, PCR, and SCR predict their structural abilities to photocatalyzed and solubilize the bio-molecules as BSA LSNR and LGT nanomaterials could also be doped and blended with a fine powder of waste plastics to functionalize and recycle them.[12] LSNRs and LGT could structurally align GO and polymer composites for wider applications as supercapacitors and metallic nanocatalysts.[8,9,13] The quantized interface ($4f^{\#e} \sim$ FE) could split light and water due to mutually resonating energy transfer for separating light.[14] Thereby, LGT depicted as $4f^{\#e} \sim$ FE could replace the expensive prisms used for splitting light for the faster photocatalysis of industrial effluents.[15] LSNRs could also be doped with proteins, chitosan, carbohydrates/cellulose as biotemplates with a $4f^{\#e} \sim$ FE interface for biophysical applications.[16] LGT with $4f^{\#e} \sim$ FE as an energy simulator could trap solar radiation for bio and piezoelectric sensors and minimize light scattering, and quantum confinements within optoelectronics.[3,17] Unlike MOFs of transition metals, the lanthanide organic framework (LOF) could fill a need for applications with higher frequency of recycling and energy storage.[18] The functional edges (FE) and π conjugations of GO with photons ($h\nu$) generates a wavefunction (ψ) in different phases (φ), but the $4f^{\#e} \sim$ FE interface photocatalyzed a dye in a shorter time with an intensified redox cycle (ROC).[15–17] LSNRs and LGT could affect salt bridges, electrostatics, and the peptide bonds of a protein by generating thermodynamic parameters tuned by $4f^{\#e}$ electrons.[18,19] GO as an $h\nu$ receptor has been a key factor in the fluorescence and photoluminescence of LGT.[20,21] The $4f^{\#e}$ align GO with the lowest permittivity (ε) and quantum energy barrier (QEB) without causing electron–electron collisions. LGT with a highly resonating frequency of $4f^{\#e}$ and GO together attain outstanding optical, luminescence, and magnetic properties with extensive screening for diagnostic applications in the biological domain.[22] LGT with balanced hydrophobicity and hydrophilicity could boost drug delivery, fluorescent probes, bioimaging, biosensors, and contrast agents in MRI scanning interaction with globular protein, but no study has been reported yet.[22–26] The $4f^{\#e} \sim$ FE interface as a new framework is aimed at separating out hazardous materials from biomedical waste effluents. PCPs of LGT suggest intensification of molecular interactions to recycle wastewater via hydrophobic and hydrophilic activities. The morphology, crystallinity, and redox activities of

LSNRs have not yet been reported.[26–28] The hydrophobic and hydrophilic interactions of $Ln(NO_3)_2 \cdot 6H_2O$ with BSA were extended to LSNRs and LGT in previous studies.[29] LSNRs and LGT could not unfold aq-BSA except by solubilising by using partial surface charges to interact with LGT. Aq-LSNR and LGT solutions align the dipoles of water that affects the adherence and cohesion of a solution with higher PCR and SCR activities interfaced with PCPs for understanding the QEB. The multifunctional LGT gets fitted with electrostatic dipoles, gaining a photon trapping ability for PCR and SCR activities. BSA interactions with partially soluble LSNRs and LGT could tune the activities of hormones and enzymes due to S^{2-} with temperature.[30] The shear stress implies a suspended BSA aligned in solution, so survismetry explores their alignments.[31] The aligned dipoles in aqueous medium catalyse the reduction of dyes via photonic and sonication energies. Therefore, the rheology, surface energy, and thermodynamic parameters have been determined as a prerequisite database for PCR and SCR activities.

2. Experimental section

2.1. Materials

Gt, H_2SO_4 (99.9%), H_3PO_4 (85%), $KmnO_4$, H_2O_2, HCl, chloride hexahydrate salts of lanthanum, cerium, terbium, holmium, sodium metal, BSA, iron sulfide, methylene blue, brilliant blue R, brilliant blue G, and methylene orange were procured from Sigma Aldrich; petroleum ether (40–60) from Sisco Research Laboratory (SRL) India, and absolute alcohol from SCVUS Mandli India, and the solutions were prepared in Milli-Q water weighed using a $\pm 1 \times 10^{-6}$ balance.

2.2. Preparation of GO and GtO from Gt

Graphite oxide (GtO) and GO were synthesized from Gt flakes with $KmnO_4$ and $H_2SO_4 : H_3PO_4$ in 8.5 : 1.5 ratio poured dropwise into an RB flask placed on an ice bath containing Gt and $KmnO_4$ in 1 : 6 ratio. These were refluxed at 55 @650 rpm in an oil bath for 12 h to reach RT. To obtain pure GtO, ice-cold water was mixed with a reaction mixture on adding 3 mL H_2O_2 (30%) and stirred for 10 min to cease a reaction.[5] The resultant product was centrifuged at 8000 rpm for 10 min and washed with Milli-Q water, HCl and absolute alcohol until the supernatant attained pH 7. $AgNO_3$ and $BaCl_2$ tests ensured complete removal of NaCl and Na_2SO_4 after 5 washings, and a brownish sediment was coagulated with petroleum ether. It was extracted to a Petri dish for drying at 60 for 24 h, a brown-colour solid GtO was obtained with good reproducibility and feasibility after repeating the procedure several times. GtO was exfoliated by sonicating at 28 kHz for 3 h to disrupt the ABAB sheet stacking of the Gt layers. GtO disperses brownish GO homogeneously[39] (Fig. 1 and 2). The reaction possibly occurs as follows:
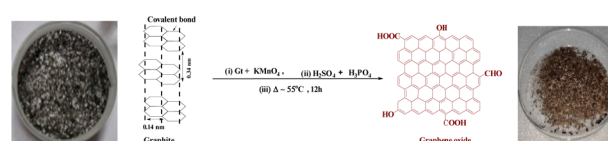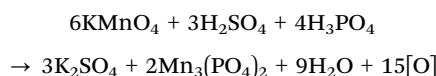

Fig. 1 GO preparation from Gt flakes.
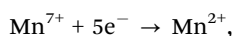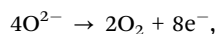
Fig. 2 LSNR preparation.

GO functionalization

$$6KMnO_4 + 3H_2SO_4 + 4H_3PO_4$$
$$\rightarrow 3K_2SO_4 + 2Mn_3(PO_4)_2 + 9H_2O + 15[O]$$

and

$$KMnO_4 \rightarrow K^+ + Mn^{7+} + 4O^{2-},$$

$$4O^{2-} \rightarrow 2O_2 + 8e^-,$$

$$Mn^{7+} + 5e^- \rightarrow Mn^{2+},$$
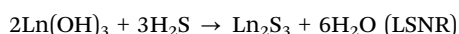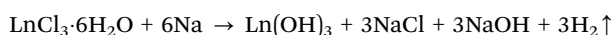
$$Gt + 15[O] \rightarrow GtO,$$

$$GtO + \cong \rightarrow GO$$
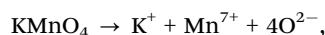
### 2.3. Crash reaction methodology (CRM) for LSNR synthesis

Crushed Na metal taken in a boiling tube was heated to 50 °C for ~1 min, then $LnCl_3 \cdot 6H_2O(s)$ was added in 1:6 ratio. It sparked the production of H_2 gas and $Ln(OH)_3$ within nanoseconds, and the mechanism is denoted CRM.[40] To solubilize $Ln(OH)_3$, water in 1:4 ratio was added to homogenize the solution (Fig. 1). An excess of H_2S gas as a source of S^{2-} was passed (10 min) to react with Ln^{3+} to produce Ln_2S_3. The H_2 gas, NaCl and NaOH were confirmed with gas chromatography, $AgNO_3$ and phenolphthalein, respectively (Fig. 3). The $3s^1$ Na reacted with $6H_2O$ to disrupt its dipolar linkage with Ln^{3+}, generating H^+ that received $3s^1$ as $2H^+ + 2e \rightarrow H_2$ (Fig. 3) as follows:

$$LnCl_3 \cdot 6H_2O + 6Na \rightarrow Ln(OH)_3 + 3NaCl + 3NaOH + 3H_2\uparrow$$

$$2Ln(OH)_3 + 3H_2S \rightarrow Ln_2S_3 + 6H_2O \text{ (LSNR)}$$

A temperature of 50 °C ignited $3s^1$ to gain adequate oscillations which simultaneously interfaced with H_2O to dissociate it. The product was washed with Milli-Q water 4/5 times to remove NaCl and NaOH. The whitish to greenish colour confirmed LSNRs which with $AgNO_3$ had formed black precipitate implying S^{2-} (Fig. 3). Ln_2S_3 was washed 2–3 times and dried at 50 °C for 2 h in a vacuum oven.[40]

La_2S_3 ($S^{2-} = Ln^{3+}-Ln^{3+} = S^{2-}$) with $4f^{0e}$ have developed cohesive forces and with less kinetic energy have aligned to form linear rods (Fig. 4), although the white patches imply thick nanorods (NRs) due to linearly aligned S^{2-} and Ln^{3+}. The S^{2-} oscillate to align LSNRs and $4f^{\#e}$ in different φ. The double bonds of $S^{2-} = Ln^{3+}-$ and $-Ln^{3+} = S^{2-}$ and both double bonds of $S^{2-} = Ln^{3+}-S^{2-} = S^{2-}$ align linearly with the spatial lattice as NRs. The oscillation of the double bonds of $S^{2-} = Ln^{3+}-S^{2-}-S^{2-}$
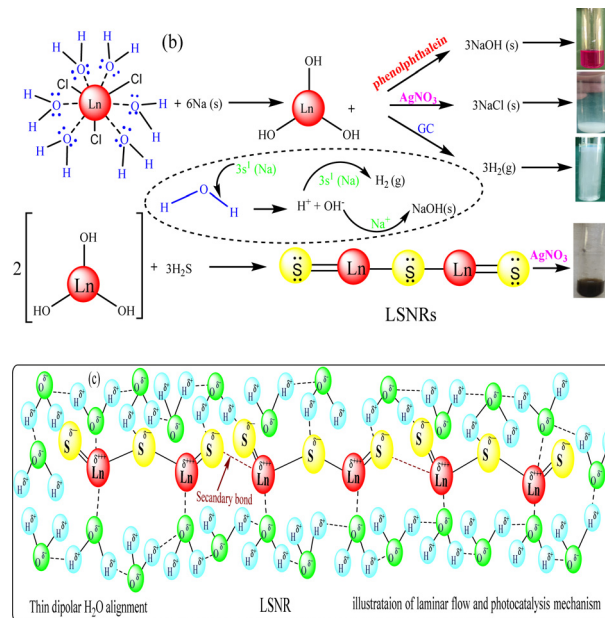
Fig. 3 (a) CRM with evolution of H_2 gas, (b) LSNR confirmatory test and (c) alignment.

affects the electronic activities of Ln^{3+} and S^{2-} due to electrostatic interactions at the terminals. There are no possibilities of charge oscillations as their ψ^2 is attained and Ce_2S_3 ($4f^{1e}$) has created a cage-like structure compared to La_2S_3 with maximum oscillations in different φ. Additionally, Tb_2S_3 with $4f^{9e}$ shows a finer distribution for developing a sheet-like arrangement. Ho_2S_3 with $4f^{11e}$ shows perfect NRs on aligning the S^{2-} with the conduction band (CB) (Fig. 4). The LSNR has one dimension (1D) due to having a wavefunction of the unoccupied state of the lone pair of electrons of the sulfur atom including its
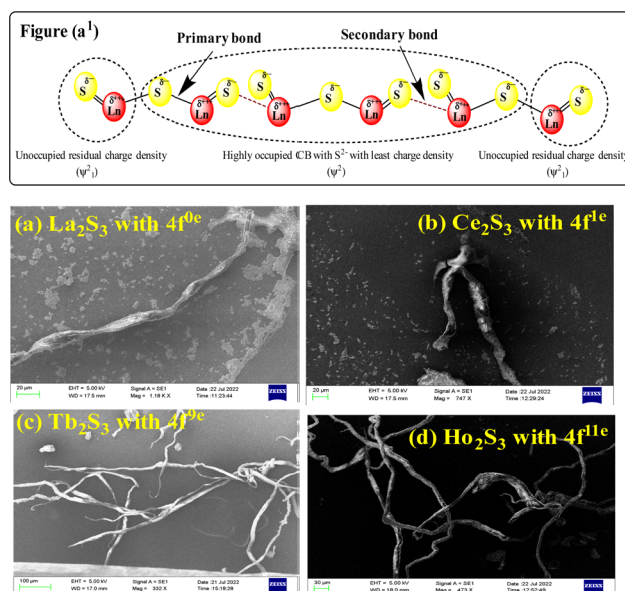
Fig. 4 (a^1) Preferred interaction for LSNR formation and SEM images (a) La_2S_3 (b) Ce_2S_3 (c) Tb_2S_3 (d) Ho_2S_3.

negatively charged domain facilitated by 4f$^{#e}$ (Fig. 4a^1). The secondary bond of Ln^{3+} and S^{2-} static ions help to equipartition their residual electronic charges through quantizing their wavefunctions, generating communication for their spatial alignment as a state. Thus, their eigenenergy and eigenfunctions generate a $\psi(x, t) \times \psi^*(x, t)$ density of energy state (DOS), which was elucidated with elemental diffraction X-ray spectroscopy and CHNS/O analysis. Our previous study of GO, Pr$_2$S$_3$–GO, Sm$_2$S$_3$–GO, Eu$_2$S$_3$–GO, and Gd$_2$S$_3$–GO used HR-TEM images with 20 nm range to infer 1D nanorods.[40] Additionally, the HR-TEM analysis of Gd$_2$O$_3$ doped with Eu^{3+} and capped with PVP functionalised with HSA maintained the nanorod dimension reported in our earlier study.[41] A similar methodology to that of LSNR and LGT was extended to the present study where the 4f$^{#e}$ of LSNR and FE of GO have been coordinated through their respective $\psi_{#4fe}$ and ψ_{FE} to initiate the $\psi_{#4fe}(x_1, t) \times \psi_{FE}(x_2, t)$ DOS. The x_1 and x_2 positions of the 4f$^{#e}$ and FE, respectively, differ infinitesimally to generate ($q^{#4fe}$, q^{FE})/$4\pi\varepsilon r^2$, as the intermixing distance r is approachable. These highly inclusive electronic states, as per the Born–Oppenheimer approximation, optimize and simulate the electronic and nuclear charges, leading to coordination *via* the S^{2-} ions of an LSNR with consecutive LSNRs. Thereby, the changes occur at nanometre distance, causing stacking LSNRs to stack linearly, as in Fig. 4a–d. SEM images of La$_2$S$_3$, Ce$_2$S$_3$, Tb$_2$S$_3$, and Ho$_2$S$_3$ imply linear rods. However, they have formed a bundled state on combining close to each other, but the dimension remains broadly 1D.

2.4. LGT synthesis *via* sonothermal process

GO (mg mL^{-1}) was sonicated for 3 h to disperse the sheets in water to generate FE (Fig. 5a). LSNR powder in GO solution with 1 : 5 ratio (dopant : matrix) was sonicated for 30 min at 60 and cooled to RT (Fig. 5). GO sheets with a floppy structure engaged with LSNRs for doping. (Fig. 5d). After the LGT was washed with H$_2$O to remove LSNRs weakly bonded with GO, it was put through a centrifuge for 8 min at 8000 rpm. The LFT was dried in a vacuum oven for 2 h at 50 as shown below:

$$GO + \cong \rightarrow GO^*, \quad GO^* + Ln_2S_3 \rightarrow Ln_2S_3{:}GO \text{ (LGT)}$$
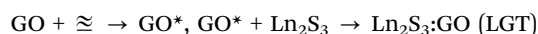
Spatial alignments and the geometrical appearance of LGT are shown in Fig. 5.

2.5. Characterizations

UV/Vis spectra were recorded with a Shimadzu UV1800 double beam spectrophotometer and X-ray diffraction (XR) with a Bruker Advance-D8 diffractometer with Cu Kα radiation (λ = 0.15406 nm, 40 kV, 40 mA). TGA was conducted in an N$_2$ environment on an EXSTAR TG/DTA 7300 to analyze thermal stability. C, H, N, and S analysis was undertaken with a Euro-vector EURO EA 3000, and FESEM + EDS with a JEOL JSM 7100F. The Raman spectra were recorded with a Horiba HR 800 instrument with a 480 nm Ar laser. Functional groups (FGs) were analysed with an FT-IR spectrometer (PerkinElmer, Spectrum 65), H$_2$ evolution with a gas chromatograph (Perkin-Elmer, Clarus 680), and PCPs and density with a Mansingh survismeter (Cal.06070582/1.01/C – 0395,NPL,GOI) and Anton par Densimeter-5000, respectively.
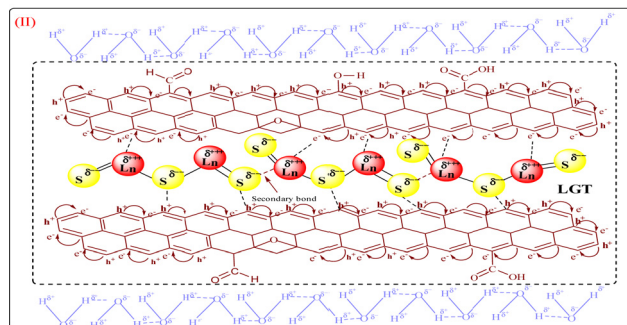

Fig. 5 (I) LGT preparation and (II) alignment.

3. Results and discussion

LnCl$_3$·6H$_2$O with a stronger nuclear charge can hold 6H$_2$O and detach 3Cl$^-$ in aqueous solution in response to AgNO$_3$. Na$^+$Cl$^-$ with H$_2$S gas developed Na$_2$S but was unable to develop Ln$_2$S$_3$. Heating LnCl$_3$·6H$_2$O could not thermally induce electronic spin to overcome a nuclear charge being applied on 6H$_2$O. LnCl$_3$·6H$_2$O reacted directly with H$_2$S gas but did not form LSNRs. The NaOH added in aq-LnCl$_3$·6H$_2$O gives NaCl and free S^{2-} to capture Ln^{3+} by weakening their inner hydration sphere (IHS). The weaker IHS of LnCl$_3$·6H$_2$O attracts free S^{2-} and forms a cloudy cluster around Ln^{3+} (Fig. 6).

Previous researchers could not analyse the electronic bonding of 6H$_2$O with LnCl$_3$ in areas of lanthanide chemistry (Table 1). LGT with 4f$^{#e}$ with a resonating energy tuned the biophysical and biochemical activities of BSA for an interfacial study extendable to haemoglobin *via* the holding/releasing ability of O$_2$ and CO$_2$ gases. Solute and solvent interaction affect various activities, where PCPs of LSNRs and LGT imply alignment to enhance the PCR and SCR. Survismetry of GO, LSNRs, and LGT in aqueous solutions through a uniform capillary has elucidated their incompressible dipoles interfaced with PCR and SCR activities. The aligned dipoles of LGT could have minimized the localized collisions of e$^-$ and h$^+$ holes by avoiding their recombination due to a robust friccohesity resonating energy transfer (FRET). In the reaction LnCl$_3$·6H$_2$O $\rightarrow$ Ln^{3+} + 3Cl$^-$, in addition to the 6H$_2$O
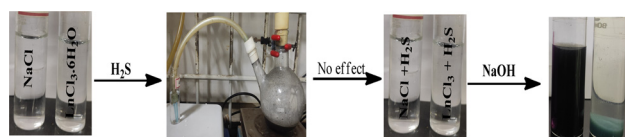

Fig. 6 Direct sulfurization with aq-NaCl and LnCl$_3$·6H$_2$O.

molecules, infinite dipoles of H_2O align with Ln^{3+}, developing the strongest electrostatic interactions. These activities spontaneously favour the generation of electron-deficient $\psi_{Ln^{3+}}$ and ψ_{OH_2} clouds. These clouds are highly stable even when dissolved in H_2O, though the $3Cl^-$ anions get dissociated, which further exceptionally reorients the H_2O dipole to optimize the negatively charged clouds of H_2O with maximum hybridization. The Cl^- had hurdled the alignments of H_2O to $LnCl_3\cdot6H_2O$, but after the removal of the $3Cl^-$, an infinite number of H_2O had surrounded the Ln^{3+}, which interfered with the bonding the S^{2-} supplied on passing H_2S. These activities are supported with $4f^{\#e}$ of lanthanide due to 5d and 6s suborbitals sharing a nuclear charge that weakens the attraction of the $4f^{\#e}$ for a nuclear charge. The dissociated Cl^- gave a positive test with $AgNO_3$ as a white $AgCl$ cloud while it was noted that strongly hydrated Ln^{3+} could not respond to H_2S or Na_2 (Fig. 6). The chemical species $Na^+ + S^{2-}$ and $H^+ + S^{2-}$ obtained on dissociation of the Na_2S and H_2S respectively could not attract the hydrating H_2O dipoles. As the dipoles were electronically bonded with $Ln^{3+}H_2O–Ln^{3+}–6H_2O$ and confined to quantum dots (QD–Ln–NHS) highly intensified with a highest energy. This energy acted as non-permissible reaction so the S^{2-} could not penetrate the QD–Ln–NHS. Hence, the large S^{2-} could not penetrate QD–Ln–NHS, so aq-Na_2S could not develop Ln_2S_3. The S^{2-} could not cause adequate spin, rotational, vibrational, or translational movement compared to a $3s^1$ electron due to the least size that could enter the QD–Ln–NHS to reduce the H_2O (Fig. 3a). The $2H^+(2H^+ + 2e^- \rightarrow H_2) + 2OH^-$ and Na^+ expeditiously develop $NaOH$. Another negative factor in using Na_2S is that it is dangerous for the H_2O molecule to develop a cationic hydration sphere. The Na metal with a $3s^1$ electron is not a danger, but rather is a highly favourable mechanism where the spin of the $3s^1$ electron gains a robust ψ to overcome a quantum tunnelling effect to separate out the hydrating H_2O dipoles. Hence, there are no electronic or vibrational energies to facilitate the Na-$3s^1$ electron reaching the QD–Ln–NHS unlike S^{2-}. The energy which is expeditiously released during the reaction excites the electron of the hydrating H_2O molecule of $LnCl_3\cdot6H_2O$ and separates it out. A precaution which is maintained to synthesize LSNRs using Na-$3s^1$ is that small amounts of both the reagents were taken. Additionally, Na_2S acquires energy from the reacting system to dissociate the $2Na^+ + S^{2-}$, which attracts the cation (CHS) and anion (AHS) hydration spheres, weakening the activities of the H_2O medium to affect the alignment of the CHS and AHS around QD–Ln–NHS, to not only immobilize the structural activities of the H_2O medium but also remove the chemical potential (μ) to develop Ln_2S_3 as $a = e^{\mu}/RT$ activities. Several reactions with Na_2S, H_2S, K_2S, Ca_2S, and others were conducted which could not produce Ln_2S_3. The Na-$3s^1$ electron is easily accessible to the $H^{\delta+}$ population and could not reduce Ln^{3+} to Ln^0 metal, avoiding the $Ln^{3+} + 3s^1 \rightarrow Ln^0$ reaction and instead consuming the $H^{\delta+}$ charges. The present mechanism is safer as almost all the H_2O molecules are either strongly hydrogen bonded where a major chunk of H_2O is hydrating Ln^{3+} and $3Cl^-$. Hence, the Na metal was warmed up to 50–55 to react with Ln^{3+}. Had there been free H_2O, there would have been a stronger reaction. Detailed studies of the CRM were

reported in our previous study.[40] Lots of trials were made to synthesize the LSNRs by avoiding a direct heating to 800–1300, as reported in earlier studies (Fig. 6 and Table 1). Developing the infrastructure for generating 800–1300 is very difficult and dangerous, unlike using Na metal. The flame shown in Fig. 3a belongs to the H_2 gas which was produced during the reaction. Of course, by developing pressure within a few seconds it is diffused. The H_2 gas was intensively confined to a flame as we wanted to confirm it with a popping sound and a yellowish flame. However, provision was made to generate Ln^{3+} by allowing contact with a small amount of Na metal by passing it through a conveyor belt to the reaction chamber and attracting the resultant Ln^{3+} to H_2S gas to develop $Ln_2S_3 + H_2$. Hence, the conveyor belt system is highly scalable.

LGT and LSNRs with a smaller surface area induce stronger interactions between the δ^- and δ^+ aligned dipoles of H_2O. The $4f^{\#e}$ of LGT oscillates with ψ and minimized ε for expeditious PCR and SCR activities of dyes, causing the uniform alignment shown with PCPs. The electrostatic dipoles of H_2O interact with monodispersed aq-LSNR and aq-LGT, so a laminar flow was studied from 0.002 to 0.10 g% @ 0.004 g% to align them (Fig. 13). The and values do not vary on increasing the g% of LSN and LG, as they could act in ordered alignment as a supercapacitor (Tables 5 and 6). The water dipoles and the aligned LSNR:GO develop a pendant drop number (pdn) saturated at 298.15 K with new surfaces (Fig. 14b). LGT formed a large size drop with increasing g% due to alignment with a more strongly adhered solution and multiple nanohydration spheres (NHSs) that isolated their cohesive forces (Fig. 6). Aq-LGT adheres to a solid glass surface by developing a pdn in continuous flow, cohesively holding a solution with an adequate cohesive force of adhered water to LGT and surrounding water molecules. This action develops the size and length of a pdn due to stronger adhesive and cohesive forces of H_2O to LGT and with itself. The lower surface area of a drop implies H_2O adhered to LGT forming an NHS around the LGT, weakening the $H_2O–H_2O$ electrostatic interactions (Fig. 7). GO, LSNR, and LGT act as competent photocatalysts to PCR and SCR fluorescent dyes in aqueous solution. On receiving $h\nu$, the surface area and surface energy, with their realignment and reorientation in the photocatalyzing liquid mixture, have become the most critical interfaces. The photocatalysts on receiving the $h\nu$ haphazardly collide, increasing the probability of holes recombining, so the $h\nu$ may not generate effective quantum dots to cause $h\nu$ to excite the electron. Hence surface enhanced Raman spectroscopy (SERS) highlights the surface activities reported in our previous study.[3,40] Additionally, due to the surface energies, the molecules develop NHSs, which could combine via the cohesive force that develops pdns of different sizes, affecting the photocatalysis. Thereby, the compositions of GO, LSNRs, and LGT generate the surface activities which influence the width of the pdn with a lower surface area. Fig. 7 shows that the 0.002, 0.004, 0.006, and 0.010 g% LSNRs respectively increase the size of the pdn. The 0.010% sample has a comparatively longer pdn due to stronger cohesive forces with slightly milder adhesive forces with a lower tip of the hanging capillary with the controlled
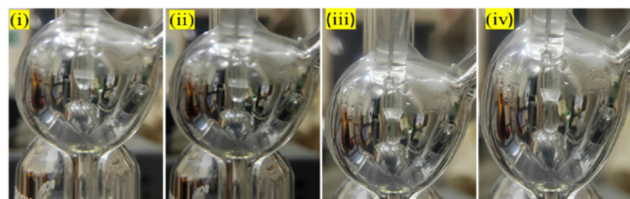
Fig. 7 Increasing size of drop with @g% due to lower surface area.

Fig. 8 XRD of (a) bare GO, (b) La$_2$S$_3$:GO, (c) Ce$_2$S$_3$:GO, (d) Tb$_2$S$_3$:GO, (e) Ho$_2$S$_3$:GO.

pressure unit (Fig. 7). This mechanism of milder adhesion, with either a concentrated photocatalyst or a dye with comparatively stronger cohesive forces, by itself increases the QEB to hamper the photocatalysis. The pdn decreases as the cohesive forces are strengthened with increasing composition, which could reduce the quantum yield (Fig. 7).

GO has been synthesized and widely characterized with XPS, XRD, TGA, HR-TEM, SEM, and EDX reported in our previous studies.[42] Widely and vividly reported studies suggested that GO has a 2D sheet structure with hexagonal units with moderate VWF. GO has been functionalised by generating oxygenated FGs, which further realigned the 2D GO sheet with slightly different intersheet VWF causing the lowest relaxation time. These structures have been extensively studied with stretching frequency and bending frequency (Fig. 9 and Fig. S2.9, ESI†). The FT-IR analysis for LSNRs and LGT individually elaborated the spatial geometry with specific rotational, vibrational, and electronic motions integrated as stretching and bending frequencies. The C–C–C atomic domains of LGT for 1900–3000 cm^{-1} are almost linear compared to a GO matrix, which indicates the activities of the FGs. These activities were minimized and FGs were used in doping the LSNRs. But dopants with specific doping activities to tune the C–C–C atomic domains are lacking for individual LSNRs (Fig. S1.1, ESI†). The S–S atomic oscillations are depicted with the pattern of split of stretching and bending frequencies where the integrated 2D GO sheet with highly stable C–C–C atom domain that could not split the stretching and bending frequencies. These fundamental patterns exclusively elucidate the structure of GO, LSNRs, and LGT. Intrinsic friccohesity correlates the stretching and bending frequencies of GO, LSNRs, and LGT as the intrinsic electronic configurations of each adjoining atom rotate, vibrate, and translate with specific oscillations. These generate specific patterns of electron–electron repulsion, electronic collision, and mean free path, as per Lorentz activities. These oscillations generate a specific pattern in TGA, DTG, and DSC (Fig. 10). GO generates a single sharp line reflecting its single lattice structural pattern. However, the single sharp line is transformed into different patterns with the LSNR spatial lattice, implying that the 4f$^{\#e}$ of LSNRs seem to coordinate for mutual optimization. Hence the specific patterns of the LGT differ from those of GO with faster photocatalyzing activities. These changes imply the participation of the FGs of GO and the 4f$^{\#e}$ of the LSNRs due to their structural alignments. FT-IR and TGA analyses have extensively elaborated the originality and functionality of their structures, developing specific patterns of wavevector and lattice, as depicted by the XRD pattern (Fig. 8).
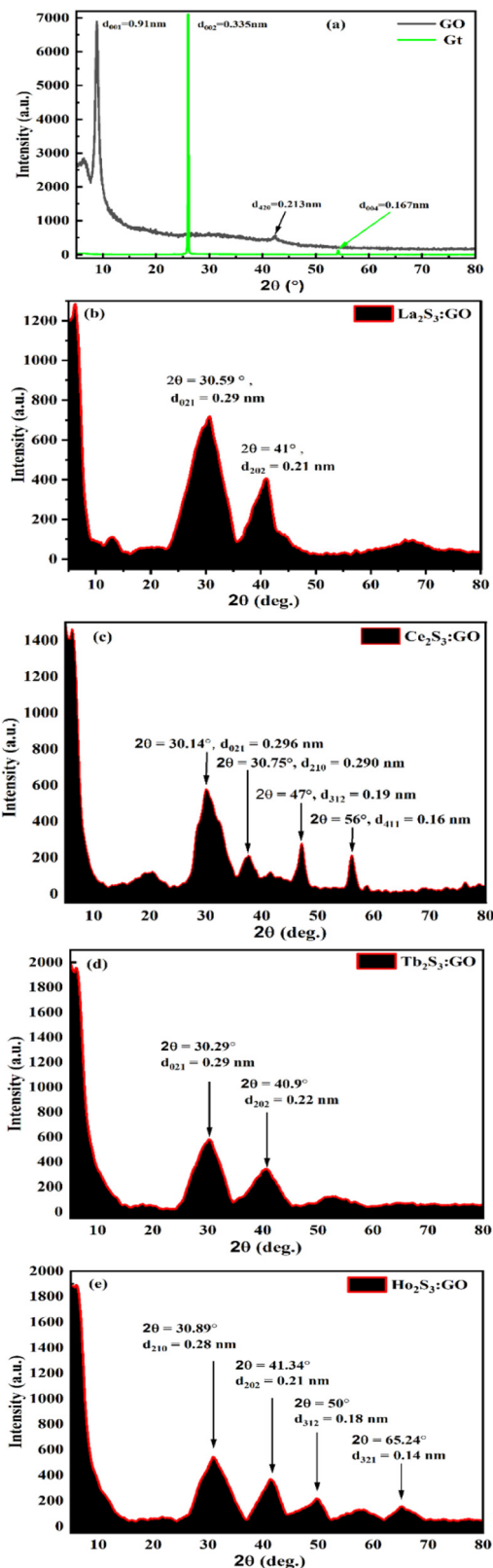
Table 2 Elemental composition analysis for LSNR, GO, and LGT

Sr. no.	Name	C (%)	H (%)	S (%)	Weight (mg)
1	GO	60.558	3.306	—	1.0752
2	La_2S_3:GO	18.782	2.669	2.134	1.0756
3	Ce_2S_3:GO	20.915	1.799	2.642	1.0995
4	Tb_2S_3:GO	19.264	2.480	1.764	1.0299
5	Ho_2S_3:GO	25.024	2.475	1.964	1.0295

Table 3 Elemental composition *via* EDS for LSNRs, GO, and LGT

System	Element	Weight (%)	Atomic weight (%)
Tb_2S_3	Tb	88.24	60.23
	S	11.76	39.77
Ho_2S_3	Ho	97.17	86.97
	S	2.83	13.03
GO	C	69.57	75.28
	O	30.43	24.72
Tb_2S_3–GO	C	55.90	64.10
	O	40.42	34.65
	S	1.04	1.02
	Tb	2.64	0.23
Ho_2S_3–GO	C	56.19	63.84
	O	41.23	36.01
	S	1.01	0.06
	Ho	1.57	0.13

The specific characteristics of GO and the lattice are depicted with XRD. The specific features express the GO skeleton doped with LSNRs, as depicted with an XRD pattern for each LGT (Fig. 8). The XRD pattern of GO differs from that of the LGT which authentically indicates the doping mechanism due to the interaction and optimization activities of the FGs and $4f^{\#e}$ of LSNRs. Thereby, FT-IR, TGA, and XRD depict the structural lattice and features expressed as an energy spectrum denoted as DOS. These specific structural patterns supported by specific patterns of their morphology are depicted with SEM. The DLS data and distribution patterns of GO and the LGT in a most controlled pattern indicate the structural morphology and topography, which further synchronize their interacting PCP profiles. Structural illustrations focussing on almost each and every atom and their linkages in GO, LSNRs, and LGT indicate the stability of their structural frameworks despite subjecting them to photons. The elemental analysis further gives their structural constituents and their ratios to predict their presence in the structural lattice (Table 2). EDX spectroscopy was run on the samples, which elucidated their structural frameworks with their elemental composition (Table 3). Reports of our previous study with LSNRs and LGT of Pr_2S_3, Sm_2S_3, Eu_2S_3, and Gd_2S_3 included XPS that confirmed the elemental composition and participation of each constituent stabilizing their resultant lattices.[40]

3.1. X-ray diffraction analysis

The single sharp GO peak at $2\theta = 8.83°$, despite treatment with Gt, means a stronger oxidising mixture could not disrupt the

covalent bond between C atoms, but it weakened the van der Waals forces (VWF) binding the GO sheets. The GO matrix accommodated a lesser amount of LSNR dopant due to $4f^{\#e}$ in the doping[43] (Fig. 8a–e). The Gt plane at (002) is shifted to (001) in GO due to the intersheet distance (Fig. 8a, green line). LSNRs with LGT has reduced the intensity of minor peaks from 7000 for GO to 2200 for LGT8. The LGT generates a new intensity due to ROC of h^+ and e^- holes resulting in lower intensity (Fig. 8a–e). XRD suggests there is no dissociation, with stronger interatomic forces generating prominent peaks at $2\theta = 30.59°$ and $41°$ for La_2S_3:GO with 0.29 and 0.21 nm d-spacings, respectively.[27] While Ce_2S_3:GO has peaks at $2\theta = 20°$, $30.14°$, $30.75°$, $47°$ and $57°$ with 0.443, 0.296, 0.290, 0.190 and 0.160 nm d-spacings of the lattice plane, respectively.[44] This has direct implications for PCPs, as a lattice plane develops different NHSs according to the d spacing. This indicates the relevance of PCPs to PCR and SCR, as the alignment of water affects electronic transitions. Tb_2S_3:GO with five half-filled electrons from the valence band (VB) to the conduction band (CB) causes the maximum number of collisions, unlike Ce_2S_3:GO, which generates sharper peaks at $2\theta = 30.29°$ and $40.9°$ with d-spacings of 0.29 and 0.22 nm. Ho_2S_3:GO has peaks at $2\theta = 30.89°$, $41.34°$, $50°$ and $65.24°$ with 0.28, 0.21, 0.18 and 0.14 nm d-spacings, respectively, with $4f^{11e}$ with four CBs that split into multiple peaks after with robust collisions, while the GO sheet remains structurally intact. LGT aligned with different peaks as GO is aligned at $2\theta = 8.83°$ with 6900 a.u. The FG synchronizes with a continuous electronic plane to interface the $4f^{\#e} \sim$ FE collisions. The electronic configurations with higher d spacings for GO suggest stronger reducing activities as the FG might have pushed the LSNRs into the GO intersheet due to a higher mean free path (Fig. 8).

3.2. FT-IR analysis

The bands at 3375, 1726, 1167 1051 and 1625 cm^{-1} for the stretching of –OH, –COOH–C=O, C–O–C and OH, respectively, come GO alone (Fig. 9a). These FGs are aligned with different intensities around the various paths developing different lattices (Fig. 8). Their geometries influence the shear and surface energy for a PCP sensor. The bending vibrations of –OH, epoxide (–O–), and the skeletal rings of GO occur at 1624 cm^{-1} with a small stretching vibration hump at 1372 cm^{-1} from tertiary C–OH. The PCPs have repeated their state functions for conversion into the resulting product. The LGT has aligned the GO sheet to quench undesirable $\pi \rightarrow \pi^\star$ transitions of FGs and residual potential charges. FE exists with Ce_2S_3:GO and d-spacing with the restrictions, unlike Tb_2S_3:GO and Ho_2S_3:GO with $4f^{9e}$ and $4f^{11e}$, respectively. A new band at 1633 cm^{-1} indicates LSNR:GO optimization by FGs and $4f^{\#e}$ transitions. The stretching depends on electron–electron repulsion of $4f^{\#e}$ with nuclear charge.[36] The Born–Oppenheimer approximation optimizes LSNRs *via* $4f^{\#e} \sim$ FE clouds on the metal surfaces. The S^{2-} of LGT might not have stretched except for a minor simulation, as stretching from 2000 to 3000 cm^{-1} indicates the C–C, C–H, C=C, and aromatic ring of LGT (Fig. 9). The stable GO sheet with prominent peaks decreases the stretching intensity. Multiple
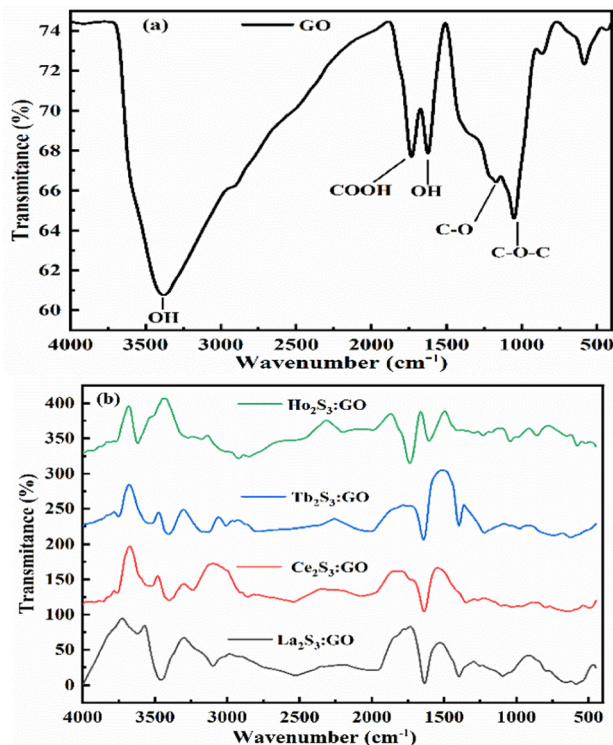
Fig. 9 FT-IR spectra analysis: (a) GO, (b) LGT.

splits in stretching indicate the collision of $4f^{\#e}$ on interacting with an electronic cloud of FE (Fig. 9). The stretching of an FG with milder peaks within 500–1000 cm^{-1} for La$_2$S$_3$:GO, Ce$_2$S$_3$:GO, Tb$_2$S$_3$:GO and Ho$_2$S$_3$:GO indicates GO doping with LSNR dopants (Fig. S2.9, ESI†). C–C is stabilized as FGs attached to the C atom are aligned to accommodate the dopants.[40]

3.3. C, H, N/S analysis

The structural changes are supported by the spatial arrangement of the constituent elements in the highest reproducible primitive lattice as a uniform wavevector of C, H, and S detected with a C, H, N, and S analyser, while the constituents of LSNRs and LGT are detected with elemental diffraction spectroscopy (Tables 2 and 3).

3.4. FESEM with EDS analysis

The morphologies of GO, LSNRs, and LGT have already been explained with SEM (Fig. 14). There is a further explicit focus on morphology with FESEM including elemental diffraction X-ray spectroscopy to explore their nucleating frameworks, elucidating their most primitive alignments (Fig. 10). Their morphologies elucidated their surface profiles at 1 μm, 10 μm, and 100 nm for GO, LSNRs, and LGT. The LSNR morphology suggests workable structural frameworks that constitute the specific atomic bonding and the sheet arrangements (Fig. 10B and D). GO constitutes the most symmetric and synchronized 2D sheet, closely interfaced with moderate VWF or Lennard Jones potential, as per the Prigogine intrinsic entropies and the Born–Oppenheimer approximation. The morphology which was further elucidated
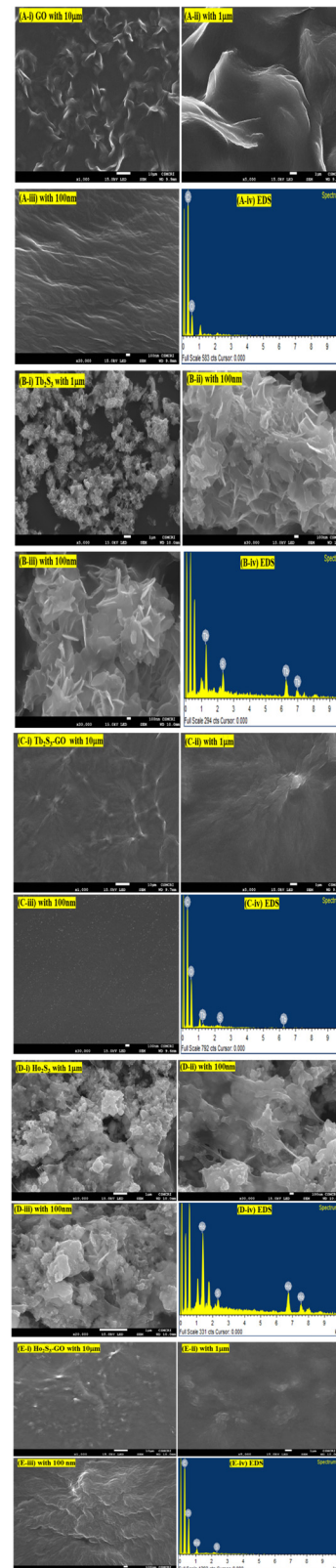
Fig. 10 The morphologies of GO, LSNRs and LGT obtained with an X-ray spectrometer (A, i–iv) GO, (B, i–iv) Tb$_2$S$_3$, (C, i–iv) Tb$_2$S$_3$:GO, (D, i–iv) Ho$_2$S$_3$, (E, i–iv) Ho$_2$S$_3$:GO.

with a 1 μm highly expanded view of the 2D GO sheet could be defined as top-to-bottom and bottom-up with a few areas and edges sharply diffracting laser light. Hence, this is a bottom-up tentropic surface with comparatively localised and ordered surface entropies within the closest interlink to resonate their energies for mutual transfer with single-valued ψ, enabling a PCR. The front view of the 1 μm scale morphology further indicates synchronized 2D GO sheets with the most symmetric upridges noted as basement spaced 2D GO sheets able to sense each minimum temperature and pressure fluctuation. These have been highly resolved at a scale of 100 nm; however, the longer 2D GO sheet with a structure similar to a carbon-fibre-like structure also reflects laser light (Fig. 10A). One side of the 2D GO fibrous sheets are anchored or adhered to a longer with few layered sheets. These sheets are highly and constantly fixed with their C atoms obtaining the 100% hybridization of potential energy *via* $|\psi_{c-1}|$, $|\psi_{c-2}|$, $|\psi_{c-3}|\ldots|\psi_{c-n}|$ = 100% hybridization. The index n indicates the number of C atoms. Hence, 2D GO fibrous sheets slightly differ in an equipartitioning of energy, where their residual energies seem to facilitate a well-defined ordered tentropy with explicit friccohesity chemistry by balancing the PE of the basement sheet and the KE of fibrous sheets developing a remarkable interfacial φ to equilibrate the $\varphi_{Fibrous} \times \varphi_{Basement}$ matrix to balance a higher stability with definite FEs and hexagonal sheets. Therefore, $|\varphi_{Fibrous}| \approx |\varphi_{Basement}|$ develops an energetic way of sticking to the higher surface area that could act as an anticoagulant, obeying autocatalytic friccohesity interfacial restrictions.

The morphology of the GO differs from LSNRs, as LSNRs could not act as 2D sheets, but rather act as one-dimensional entities with more residual energies at the terminal $3S^{2-}$ and $2La^{3+}$. These spatial DOS could align them in a 3D energetic expression of LSNRs due to residual or electron-rich and charged defect-rich domains (Fig. 4a^1). These defect-rich domains occupy the spatial dimension with $\psi_{S^{2-}} \approx \psi_{2La^{3+}}$ within the energy clouds of S^{2-} and La^{3+}. These develop a cloud-like DOS with specific virtual wavevectors where the real nanorod alignments of these LSNR entities stabilize them (Fig. 10B and D) expressed as the Schrödinger equation:

$$E_\psi = [p^2/2m + V(x, t)]\psi \tag{1}$$

E is total energy of $4f^{\#e}$ and ψ is the wavefunction, p is momentum, m is mass, and V is the potential energy (PE) at position x at time t. The position x at time t remains synchronized to symmetrize the alignments of the LSNRs. Positions x_1, $x_2, x_3,\ldots,x_n$ align symmetrically with virtual boundaries. Hence, Tb^{3+} with $4f^{8e}$ probably strengthens the bonding with S^{2-} (S_{16} = $1s^2$, $2s^2$, $2p^6$, $3s^2$, $3p^4$) where $3p^4$ has UNPE $3p_x^2$, $3p_y^1$, $3p_z^1$. Hence, the electronic activities of $3p^{4e}$ (S) and $4f^{8e}$ (Tb) lead to the development of very functional interfacial adherence with highly optimized energies from 10 μm and 100 nm (Fig. 10B). The most novel alignment of the ψ is $\psi_n = \sqrt{a/2} \sin(n\pi x/a)$, where the ψ could have $\pi/2$, π, and 2π coordinates of the wavevector. Hence, these hardcore wave mechanics laid down a function of interfacial alignment of the LSNRs and 2D GO

sheets (Fig. 10). Therefore, the LGT attained a matrix with the most QDs, highly integrated with the uniformly distributed lattice of the LSNR $\approx$ GO energy plane without disrupting the basic structural framework of the LSNRs and GO. In fact, at 100 nm scale highly uniform energetic ODs are seen without energy spreading. Hence, the $\psi_{LGT} \approx [\partial p^2/2m \pm V(x, t)]\psi$ integrate with the most synchronized arrangement depicted with the sharpest single light order.

These are compared with Ho_2S_3:GO having $4f^{10e}$ without QD rates, where the most symmetric sin waves are depicted (Fig. 10E). Hence, the electronic cloud of $4f^{10e}$ influences the QDs of GO. The elemental compositions of GO, LSNRs and LGT are included in Table 3.

3.5. TGA, DTG and DTA/DSC analysis

Ln_2S_3:GO responds to a rising temperature due to oscillation of $4f^{\#e} \sim$ FE interfaces: see the overlapped DTG and TGA curves of LGT with weight (wt) loss in three steps (Fig. 11a–d). La_2S_3:GO decomposes at 100, 221 and <800 with 20.77, 15.96 and 63.27% wt losses due to moisture, and single-bonded and double-bonded S^{2-} with LGT surfaces, respectively. A maximum decomposition rate at 204 with a sharp exothermic peak predicts that La_2S_3 will interact strongly with the FEs of GO. The La_2S_3:GO and e^-–h^+ interfacial energy optimized as $q^+q^-/4\pi\varepsilon r^2$ weakens ΔH release. Ce_2S_3:GO at 215 and 717 lose maximum weight with sharp exothermic and endothermic peaks as $4f^{1e}$ interacts with FE, causing higher stability than GO (Fig. 11a). There are 27.4, 24.74 and 47.86% wt losses of Ce_2S_3:GO at 138, 246 and <800, respectively (Fig. 11c). Tb_2S_3:GO with 20, 31.46 and 48.54% wt losses at 119, 235 and <800 has sharp peaks with maximum decomposition rate at 92 and 212, respectively. Synchronized LSNRs and GO of LGT with a few new weight losses indicate their interfacial activities. The $4f^{9e}$ synchronized electronic cloud of Tb_2S_3:GO and Ho_2S_3:GO with $4f^{11e}$ as a single crystal equalizes the PE to KE. Two sharp exothermic peaks indicate maximum energy release on interaction with GO due to its aligned FGs.

The $4f^{9e}$ of Tb_2S_3 with GO enhanced LGT stability (Fig. 11d). The maximum decomposition of Ho_2S_3:GO at 190 with a sharp exothermic peak through 79.83 and 20.17% wt loss does not suggest a crystalline structure. Ho_2S_3:GO shows a sharp weight loss at 198.19, as Ho^{3+} strongly aligns H_2O dipoles as well as FE interfaces. Therefore, Ho_2S_3:GO reduces dyes in a shorter time by minimizing the collisions to increase the mean free path to overcome the QEB (Fig. 11e). The $4f^{\#e}$ enhance the thermal stability of both LSNRs and LGT by reducing the PCR time due to having a similar FE to GO (Fig. S1.0 and S1.1, ESI†). The difference in weight loss between LSNRs and LGT suggests stability due to doping. LSNRs alone lose weight in two steps due to the two strong interfacial forces of $2Ln^{3+}$ and $3S^{2-}$. One is under the control of $4f^{11e}$ of Ln and the other under the control of S^{2-} compared to LGT with thermal stability enhancing PCR and SCR activities. The LGT loses weight in three steps due to the interfacial domains of LSNRs and GO including their electronic clouds. GO which has a C–C lattice with equal heat capacities is disrupted at 193 with 82% wt loss with a sharp
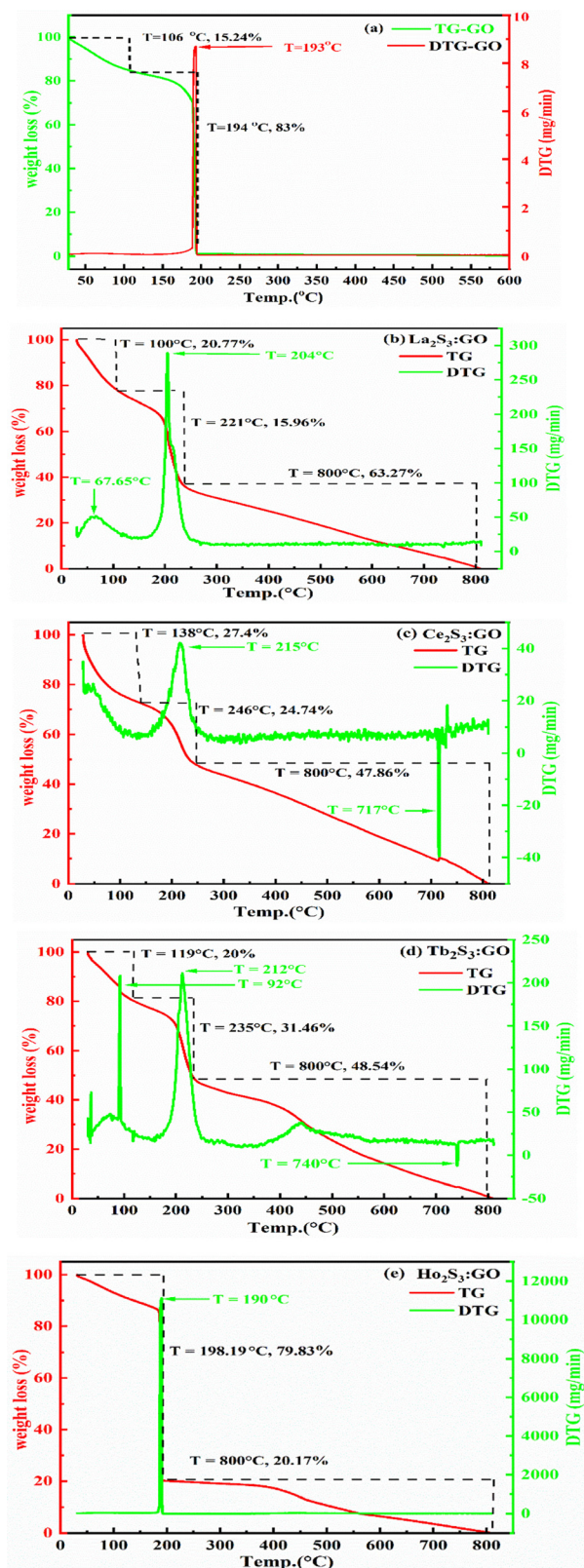
Fig. 11 TGA and DTG of GO and LGT.

peak. LSNR decomposition suggests the role of $4f^{\#e}$ by aligning the lattices of La_2S_3, Ce_2S_3, and Ho_2S_3 but not Tb_2S_3 which has a minor simulated weight loss with increasing the $4f^{\#e}$ (Fig. S1.0 and S1.1, ESI†) as:

$$T = \frac{\left(v + \frac{1}{2}\right)h}{2\pi}\sqrt{\frac{k}{\mu}}, \ \mu = \frac{m_1 m_2}{m_1 + m_2} \quad (2)$$

here $v \propto T$, $T \propto \frac{1}{\sqrt{\mu}}$ and $T \propto \sqrt{k}$, and frequency depends on temperature and oscillations as per Hooke's law, and for the bond constant k, $T \propto \sqrt{k}$.

The basic structural units of LSNRs and LGT have been expressed on by subjecting them to the XRD and TGA, as their electronic DOS respond to the laser as per according to their wavevectors. The weight of a well-defined lattice also responds to the thermal energy, which induces the oscillation to transfer the oscillating energies *via* FRET with a 1st first-order weight loss transfer rate. Thus, the TGA and DTA also define the energy changes based on a the nature of the electron–electron collision (EEC) and electron–electron repulsion (EER) that interfere with the development in the same φ in the same φ (Fig. 12, green line). Thermal energy excites the unpaired electron within the wavevector with the patterns of the DOS of the DTA peak with LSNRs with comparatively sharper apex DTA along with differential heat flow, −7.0 to 10, −0.4 to 14, −7.0 to 12, and −0.4 to 13 μV for La_2S_3, Ce_2S_3, Tb_2S_3 and Ho_2S_3, respectively, at 400 °C apex temperature (Fig. S3.5, ESI†). Thus, the lattice of the LSNRs that responded at 400 °C remained fairly much the same that responded at 400 °C. However, the sharper DTA apex for an LGT is broader without any sharper peak-like shoulder. The DTA apex is broader than that of the LGT, which proves that the LSNRs have been fairly doped with into the 2D GO 2D sheet. These structural changes have fastened an energy flow within the LGT lattice on receiving the $h\nu$ without causing the EEC and or EER by avoiding the recombination of the holes. Therefore, no the lack of a transitional peak in the DTA of LSNRs, GO, and LGT have inferred indicates smaller heat energy flow as equipartitioning the energy is equipartitioned (Fig. 12, green line). Initially LGT gains heat energy to get begin to oscillated and become ordered, where almost all the lattice points acquire a relaxation time. The unit becomes ordered within the coordinates of the initial state except the excited electronic state or the DOS. There is heat energy transfer without a loss and the PCR done is enacted as the gained heat excites an electron with a similar pattern where the $h\nu$ could also push the electron within the a similar framework with to $\psi_{Nor,T} \to \psi_{Ref,T}$. The DTA analysis for LSNRs is included in the ESI† (Fig. S3.5).

3.6. Raman spectra analysis

The laser light interacts with the molecular vibrations in GO as well in LSNR:GO that inferred from two sharper peaks in the same range of Raman shift. The ratio of D and G bands infer indicates the participation of LSNRs in the GO sheet, and
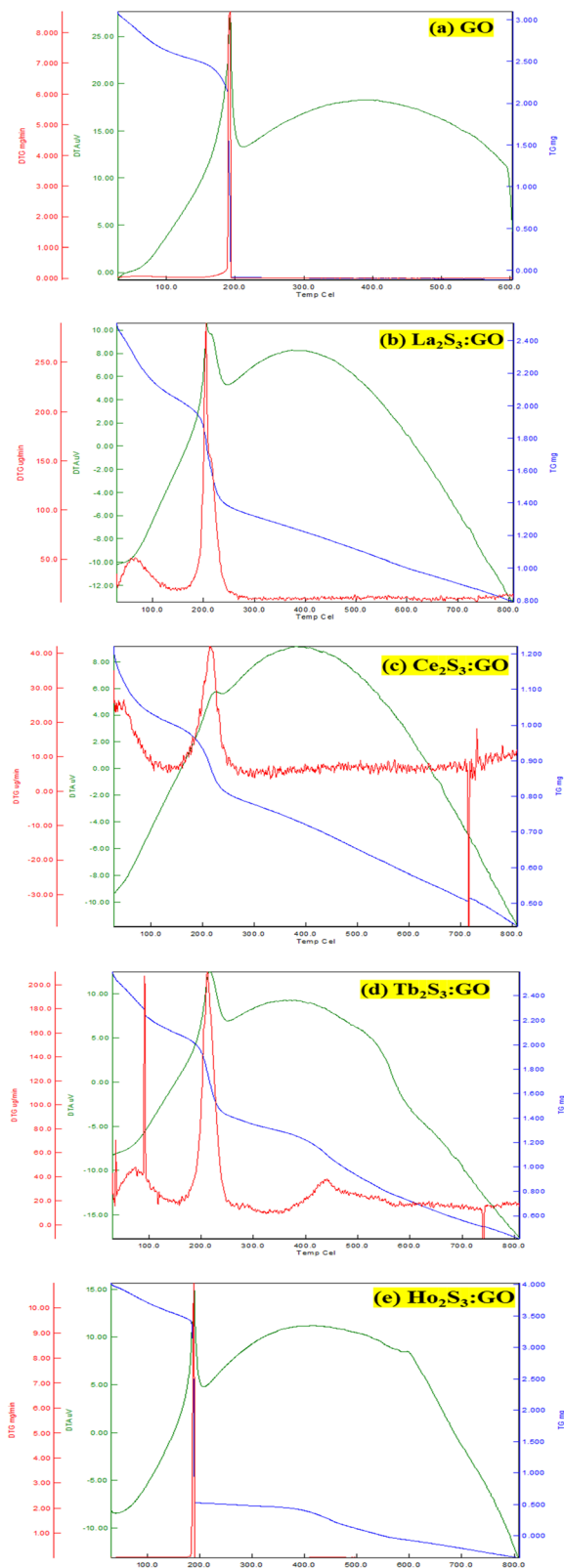
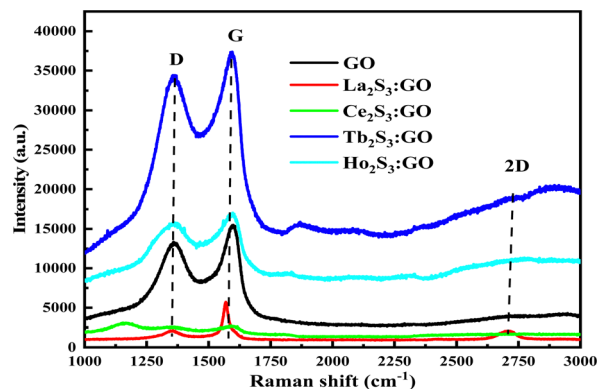Fig. 12 Differential thermal analyses: (a) GO, (b–e) LGT.

Fig. 13 Raman spectroscopy with D, G and 2D bands for GO and LSNR@GO.

Table 4 Raman shifts with D and G, bands with their ratio for GO and LGT

LSNR@GO	D-shift (cm^{-1})	G-shift (cm^{-1})	I_D/I_G
GO	13 180	15 152	0.87
La$_2$S$_3$@GO	1827	5400	0.33
Ce$_2$S$_3$@GO	2501	2609	0.95
Tb$_2$S$_3$@GO	34 021	37 340	0.91
Ho$_2$S$_3$@GO	15 465	16 812	0.92

The D, G and 2D band peaks at 1350, 1580, and 2690 cm^{-1} respectively indicate sp^2–sp^3 and C–C stretching, respectively, and the intensity ratio shows the disorder of the GO sheet. The modulated bump on the 2D band at 2728 cm^{-1} is caused by minor reorientation, and the higher intensity of the G band indicates there are more defects in the GO sheets.[5] The shift in energy bands is caused by the direct interaction of molecules with laser light. However, for the LGT, Raman spectra and intensities indicate the lattice and energy transfer behaviour of the LGT photocatalysts during the PCR. The Raman spectra have excellently developed similar patterns of the defunct activity of the 2D GO sheet doped with LSNRs in a most ordered manner (Fig. 13), as the D and G bands for GO, La$_2$S$_3$:GO, Ce$_2$S$_3$:GO, Tb$_2$S$_3$:GO and Ho$_2$S$_3$:GO are developed at 1350, 1580 cm^{-1} with variable intensities. Thus, the basic matrix remained the same with a well-defined wavevector. The fixed wavevector of a geometry with highly ordered entropy allows the increasing 4f$^{\#e}$ to equilibrate with the FE of the GO, developing a single-valued ψ_{LGT} with negligible EEC and EER, leading to an efficient $\sim$100% FRET to dye for the PCR of a dye (Table 4).

3.7. Scanning electron microscopy (SEM)

Micrographs of GO indicate a lace-like morphology of a thin sheet of C atoms in 2D at 20 m resolution with a single distribution pattern due to synchronized FGs illustrated with PCPs that focus the alignments. A single sharp peak in the GO thermogram indicates a single crystal structure (Fig. 11a). The increasing 4f$^{\#e}$ alter the topography and FE distribution in LGT depicted with the patterns of XRD, FT-IR, TGA/DTG and DLS (Fig. 8, 9 and 15). The La$_2$S$_3$:GO fragments have reoriented due to VWF to hold La$_2$S$_3$ within sheets, creating intersheet

creating disorder with the FGs and electrostatic moieties within the matrix. The $I_D/I_G < 1$ shows symmetric deformation on the GO sheet due to packing of LSNRs (Tables 1–3).

interfaces. The LGT fragments of smaller sizes enhance surface charges with higher increasing rate of PCR and SCR compared to LSNRs and GO alone (Fig. 14a and b). Ce_2S_3 with $4f^1$ having a
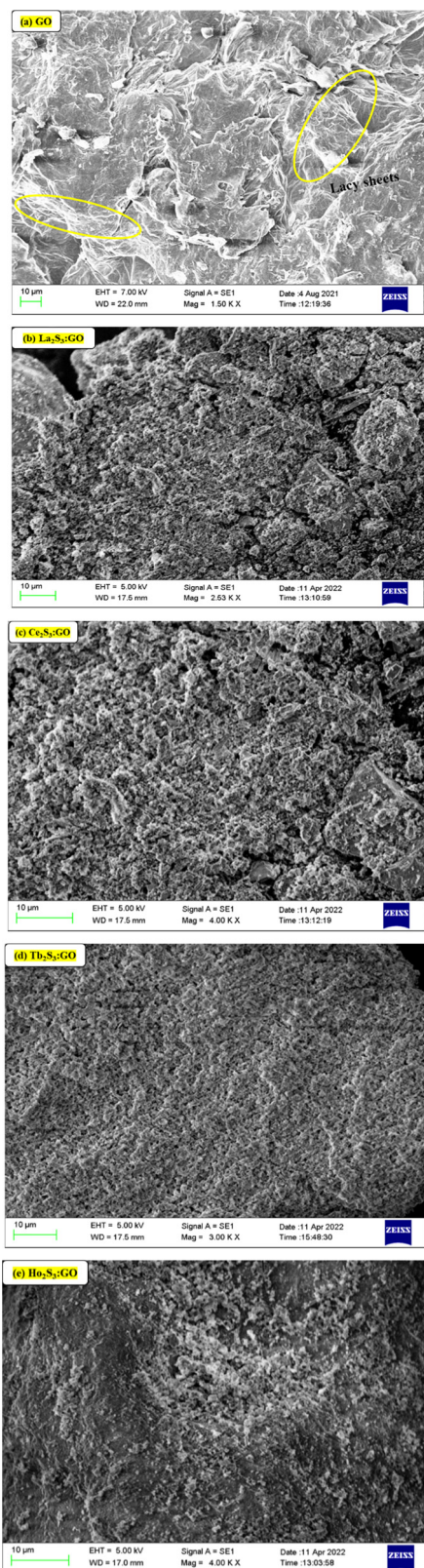

Fig. 14 SEM for surface morphology: (a) GO and (b–e) LSNR:GO.

maximum number of CB reoriented the GO sheets with the ψ in different φ and the reorienting energies spatially aligned the sheets. The upgraded ridges and furrows indicate interconnected nanorods (Fig. 4a^1). Tb_2S_3 with $4f^9$ having ψ with a highly intensified RE unlike $\psi_1 \iint \psi_2 \iint \psi_3 \iint$ unpaired electronic states with $[\psi_1 \approx \psi_2 \approx \psi_3]^2$ probability. Subscripts 1, 2, 3 on ψ denote electron transitions from $1 \rightarrow 2 \rightarrow 3$ energy states of the $4f^{\#e}$ suborbital. Critical analysis of the micrographs of GO, La_2S_3:GO, Ce_2S_3:GO, Tb_2S_3:GO and Ho_2S_3:GO indicate topographical differences at $4f^{\#e}$ (Fig. 14). The changes are caused by the splitting energy of Ln_2S_3:GO with GO due to $4f^{\#e}$. LSNR dopants have influenced the GO morphology due to $4f^{\#e} \sim$ FE on aligning a GO matrix *vis-à-vis* LGT. La_2S_3:GO, Tb_2S_3:GO, and Ho_2S_3:GO produced almost equally distributed energy patterns, unlike Ce_2S_3:GO. Equal distribution of similar lacings of GO sheets are split into equal distributions as each GO sheet participates in LGT formation. The unpaired electron of Tb^{3+} symmetrises a GO topography, accepting more $h\nu$ for PCR and SCR with Tb_2S_3:GO (Fig. 14d). Ho_2S_3 with $4f^{11e}$ develops ψ_{4f11} with the least QEB, inducing a symmetric topography RE of FE. The ψ_{4f11} and ψ_{FE} in the same φ have developed a single crystal with a sharp peak, as depicted with TDA/DTG (Fig. 11e).

Tb_2S_3:GO and Ho_2S_3:GO as robust photocatalysts and adsorbents receive maximum $h\nu$ almost in the same φ as the GO sheets for uninterrupted PCR and SCR.

3.8. Dynamic light scattering (DLS)

The $\zeta > 0$ of GO indicates aligned h^+ holes on a surface of LGT and LSNRs either from S^{2-} or Ln^{3+} charges. LGTs receive $h\nu$ with different capacities. A broader La_2S_3 distribution pattern with GO sheets indicates weaker $4f^{0e}$ interactions with FEs. The oxidation potential of La^{3+} and reduction potential of S^{2-} are unable to generate a caging of water (Fig. 15). La_2S_3 is actively distributed with less passage while on doping with GO there is maximum capping and a decrease in the passage of population on interaction of LSNRs and FEs. Ce_2S_3 with $4f^{1e}$ develops prominent collisions with a stoichiometric ratio of GO and LSNRs for LGT with a $4f^{0e} \rightarrow 4f^{11e}$ interface The conductivities of LSNRs and LGT are in the range 17 to 43 $\mu S\ cm^{-1}$ compared to the 50 $\mu S\ cm^{-1}$ of GO alone, so the $4f^{\#e}$ and FE interactions might have occupied the surface charges and mildly responded to an electrical potential with a lower mobility (Table 5). The distribution of La_2S_3 is scattered while that of La_2S_3:GO is narrow, as GO has an ordered lattice due to similar GO sheets. There is a narrower range of distribution between 100 and 1000 nm at -0.49 mV compared to that at 22.24 mV, as the La^{3+} develops Coulombic interaction with negative holes that confine C atoms (Fig. S3.4, ESI†). The redistributing electronic clouds equipartition the electronic energy of S^{2-} to interact with the h^+ holes or electron-deficient sites of GO. Their interactions have narrowed down the distribution range of La_2S_3:GO (Fig. 14). These changes are supplemented by the TGA of GO and LGT, with major structural disruption of La_2S_3 at 365 and of GO at 194, but La_2S_3:GO has elevated the GO stability of La_2S_3:GO with a major structural disruption at 221 (Fig. 11). These disruptive
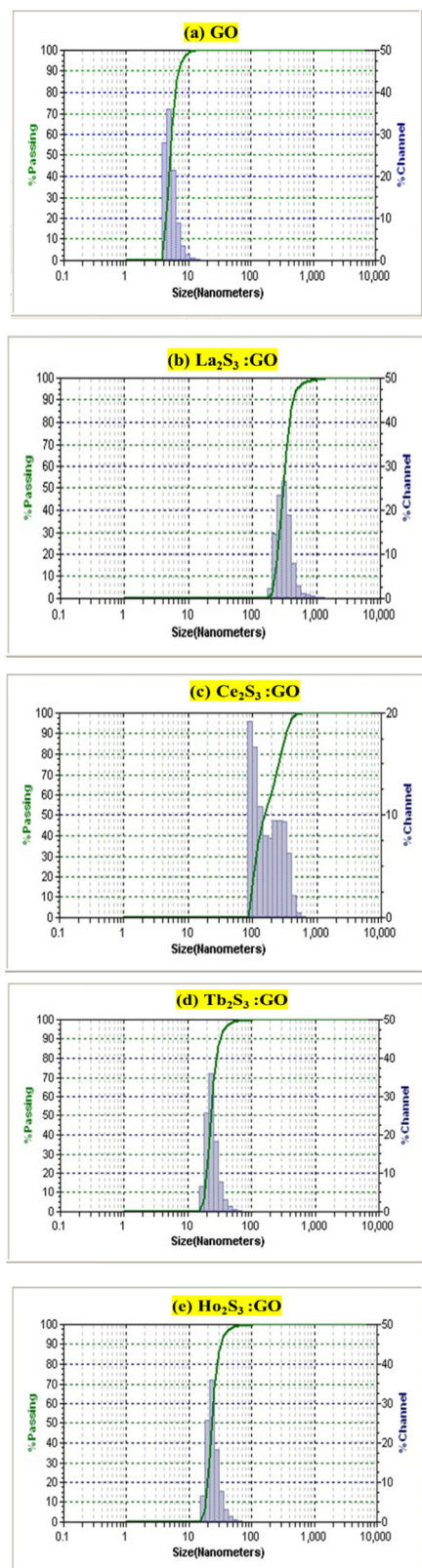
Fig. 15 Size (nm) of (a) GO and (b–e) LGT analysed by DLS.

activities indicate the doping mechanism and pattern of GO with La$_2$S$_3$. The 3e$^-$ + La^{3+} local –C–C–C– network is

simultaneously accompanied by 3h$^+$ + 3S^{2-}. The interfaces of La$_2$S$_3$ and GO narrow down the distribution range with an active state due to FRET. A similar pattern is noticed with Tb$_2$S$_3$ and Tb$_2$S$_3$:GO, as their distribution range remains almost the same with a sharp lattice disruption at 235 (Fig. 1d). Thus, the Tb^{3+}–3e$^-$ and S^{2-}–2h$^+$ electronic strings are influenced by 4f^{9e} due to their oscillations. However, the Ln^{3+}–3e$^-$ and S^{2-}–2h$^+$ loops are quantized and their localized quantum dots may be equally distributed in Ln$_2$S$_3$ and Ln$_2$S$_3$:GO. The FGs of GO could opt to interact with Ln^{3+}–3e$^-$ and S^{2-}–2h$^+$ electronic strings as Ln$_2$S$_3$:GO. Surprisingly Ce$_2$S$_3$ and Ho$_2$S$_3$ with their templates produced a fine distribution in the 10 to 1000 nm range. Ce^{3+}–3e$^-$ and Ho^{3+}–3e$^-$ with S^{2-}–2h$^+$ are simulated with 4f^{1e} and 4f^{11e} of Ce^{3+} and Ho^{3+}, respectively, which are duly supplemented with the TGA pattern (Fig. 11c and e). Since these electronic strings substantially influence their solubilizing activities, so their PCPs indicate the thermodynamic state function. The Ln^{3+}–3e$^-$(GO) and S^{2-}–2h$^+$(GO) interfaces are highly functional and localized cohesively as per their respective charges. So, solvent adherence could cause further alignment or reorientation despite their cohesiveness, and their friccohesity index could reveal a unique interaction mechanism. Ln$_2$S$_3$ and Ln$_2$S$_3$:GO have developed new interaction centres unlike the others. Their hν receiving and phonon generating activities have been found to be directly interconnected with their PCPs. Therefore, the photocatalysts were solubilized for PCP, PCR, and SCR studies. Their electronic interactions could be influenced by sonication to induce some electronic arrays in contact with 2Ln^{3+}–3S^{2-} as S = Ln–S–Ln = S nanorods. Thus, the PCPs and DLS profile elucidate applications to reduce and recycle wastewater. Ho$_2$S$_3$ has shown a 5.35 PDI which was reduced to 1.369 with Ho$_2$S$_3$:GO, as the GO capped the Ho$_2$S$_3$ around its surface. These are understood with TGA, in which it has developed multiple disruptive temperatures, but on doping developed a single crystal lattice resulting in a sharper single line at 198 against the 194 of GO (Fig. 11a and e). Ho$_2$S$_3$ has elevated the GO disruption temperature by 4. Thus, the PDI and lattice disruption *via* TGA could have a unique relationship. The diameter of La$_2$S$_3$ is 457 nm, the highest among the series, which is also explained by TGA due to the Gaussian distribution pattern of heat (Fig. 15 and Fig. S3.4, ESI†).

Except for Ce$_2$S$_3$:GO and Ho$_2$S$_3$:GO, their mobilities are almost in the same range. La$_2$S$_3$:GO and Tb$_2$S$_3$:GO have negligible ζ values, which may be due to the negative holes of GO. Their conductivity remains within 50 μS cm^{-1} and responds to electrode charges on subjection to the probe (Table 5). A detailed study of DLS for GO, LSNR and LGT is incorporated in Fig. S3.4 (ESI†).

4. LSNR and LGT solutions for PCPs, PCR and SCR

The NHSs of LSNRs and LGT with BSA could have been deformed irreversibly on acquiring unequal activation energy due to the selective charge clouds of Ln^{3+}–3e$^-$ and S^{2-}–2h$^+$
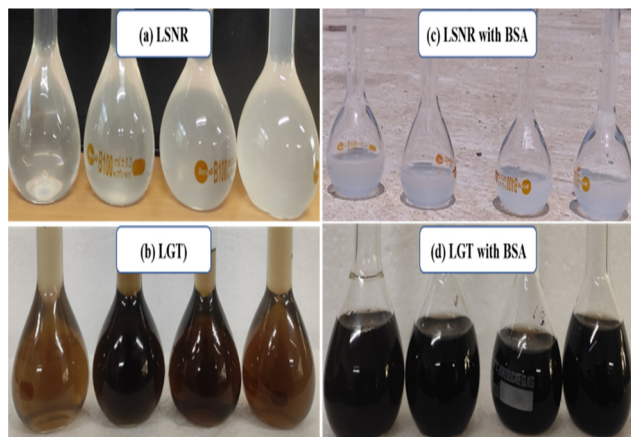

Fig. 16 Aq-solutions (a) LSNR (b) LGT (c) LSNR-BSA (d) LGT-BSA.

electronic strings with the LGT. The highly sensitive survismetry technique measures viscous flow time (vft) and pdn at 283.15 to 315.15 K.[45] Lifting a sample from a reservoir to a buffer bulb under a reduced pressure within capillaries avoided the mechanical shock that could have disarrayed the FE. A sample was equilibrated in the buffer bulb for 3 min before allowing for a backward flow to a CPU (controlled pressure unit) with a hassle-free capillary flow in survismetry.[46] PCPs for 0.002–0.010% @0.004% of LSNRs, LGT alone and with 0.010% aq-BSA at 298.15 K and 0.010% with Milli-Q water at 283.15 to 315.15 K indicate a monodispersion and structural alignment of the solution (Fig. 16a–d). LSNRs and LGT alone did not aggregate but developed a gel with BSA (Fig. 16c and d). Turbidity increases with increasing rate of g% of LSNR and LGT as $4f^{\#e}$ and FEs could align slightly, holding water molecules haphazardly. Their PCPs and thermodynamic parameters depict the solubilizing activity and interactions of aq-BSA with LSNRs and LGT. Viscosity elucidates the effect of Ln^{3+}–$3e^-$ and S^{2-}–$2h^+$ in bulk while there is a surface tension on the surfaces. These have been used as the functional interfaces to explore the activities of LSNRs and LGT for widening their applications in areas of PCR and SCR. $La_2S_3 \Delta H \ll 0$ for La_2S_3, and $\Delta H < 0$ for Ce_2S_3, Tb_2S_3, and Ho_2S_3 indicate a milder disruption of the water structure and LSNRs and LGT could have been expeditiously realigned on releasing H. Ln^{3+}–$3e^-$ and S^{2-}–$2h^+$ seem to develop stable dipoles that are explained by their photocatalyzing activities. LSNRs and LGT as a single unit with expeditious molecular motions disrupted hydrogen bonding (HB) on decreasing H and increasing S, as supported by DLS (Table 5 and Tables S1.4–S2.1, ESI†).

4.1. Density (ρ, g cm^{-3})

The ρ of LSNRs and LGT alone and with aq-BSA indicate interacting activities as a function of temperature and concentration. The ρ values are in the order of aq-BSA > La_2S_3:GO > La_2S_3:GO-BSA > La_2S_3-BSA > La_2S_3 at 288.15, 298.15 and 310.15 K, predicting stronger aq-BSA and weaker aq-Ln_2S_3 interactions. The electrostatic salt bridges of BSA strongly

attract the H_2O dipoles, including Ln^{3+}–$3e^-$ and S^{2-}–$2h^+$ electronic strings. Thus, La_2S_3 and La_2S_3:GO with aq-BSA decreased ρ by 0.039% and 0.009%, 0.039% and 0.0095%, and 0.048% and 0.16% at 288.15, 298.15 and 310.15 K, respectively as the BSA was weakly reoriented to optimize their interacting surfaces. The tryptophan and peptide bonds (PB) of BSA strongly interacted with water and Ce_2S_3:GO by occupying a majority of FEs that salted out water dipoles. BSA decreased the ρ of aq-Ce_2S_3 and aq-Ce_2S_3:GO by 0.0027% and 0.0090% at 288.15 K and 0.0026 and 0.0040% at 298.15 K, unlike the increases of 0.0029% and decreases of 0.034% at 310.15 K, respectively. Ce_2S_3:GO with increasing temperature could have generated vibrant oscillations, weakening BSA interactions with H_2O and could attract GO. BSA decreased the ρ with Tb_2S_3 and Tb_2S_3:GO by 0.006% and 0.011%, 0.007% and 0.014%, and 0.013% and 0.039% at 288.15, 298.15 and 310.15 K, respectively, as the H_2O accommodated them on holding BSA as well as Tb_2S_3 and Tb_2S_3:GO. BSA decreased the ρ of Ho_2S_3 and Ho_2S_3:GO by 0.0053% and 0.0131%, 0.0073% and 0.0160%, and 0.0073% and 0.080% at 288.15, 298.15 and 310.15 K, respectively (Tables S8.1 and S8.2, ESI†). Thus, the H_2O, which was associated with BSA, Ln_2S_3 and Ln_2S_3:GO was realigned with weaker force but adequate adherence. BSA developed stronger interactions with H_2O dipoles associated with LSNR:GO and LSNRs, with stronger internal pressure of FEs (Fig. 16). The H_2O dipoles interact with themselves and the salt bridge, and the electrostatics of BSA could have normalized Ln_2S_3 and Ln_2S_3:GO. GO engages the LSNRs in LSNR:GO via weakly interacting H_2O dipoles. The covalently bonded S^{2-} and Ln^{3+} of LSNRs and LGT develop NHSs, as NH_3^+, COO^-, >C=O, and PB along with tryptophan develop stronger hydrophilic–hydrophilic interactions (HHI), aligning LSNR:GO expeditiously during a PCR.[31]

4.2. Viscosity (η, mPa s)

The η indicating the vft of Ln^{3+}–$3e^-$ and S^{2-}–$2h^+$ aligned in aqueous solution is calculated with eqn (3) (Tables 6, 7 and Table S1.2, ESI†).

$$\eta = \left(\frac{t}{t^0}\right)\left(\frac{\rho}{\rho^0}\right)\eta_0, \quad \eta_r = \left(\frac{\eta}{\eta_0}\right)_T (1.0) \text{ and } h_r = 1 + 2.5\phi \quad (3)$$

where ρ is the density of solution, ρ^0 is the density of water, η_0 is the viscosity of water, η_r is the relative viscosity, and vft is an average relaxation time (τ). Decreasing viscosities of LSNRs and LGT alone and with BSA indicate weaker interactions due to competitive adherence with S = Ln–S–Ln = S, and aq-GO, and their interfacial charges reorient and align the NHSs, generating cohesive activities (Tables 6, 7 and Fig. 17). The η values in the order La_2S_3 > Ce_2S_3 > Tb_2S_3 > Ho_2S_3 with increasing the $4f^{\#e}$ and temperature indicate that electron spin via electron–electron collisions weakens H_2O adherence, promoting coherence. The stronger interaction of GO with Ho_2S_3 engages almost all the FEs, with stronger H_2O adherence increasing η values. The η values for LGT decreased on the GO and LSNRs mutually interacting via their respective NHSs. The NHSs align, generating mutual cohesive forces with sharply weakening adherence of H_2O, as cohesive activities induce continuity,

equilibrating the adhered H_2O as bulk H_2O. Thereby monolayer adherence of H_2O with comparatively weaker coherence
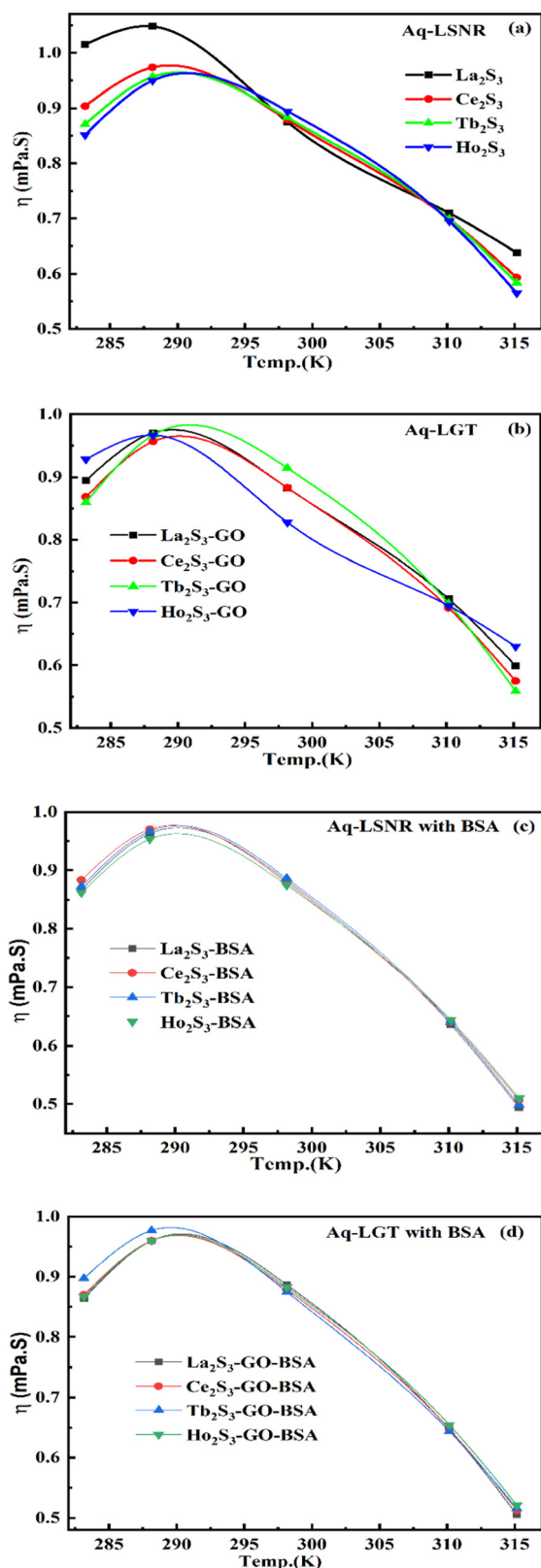

Fig. 17 Viscosity of aq-LSNR and aq-LGT with BSA at 5 T.

enhances the η at lower temperature. These activities sensitively visualised a change compared to an uneven magnitude of γ data at higher temperature (Fig. 17c and d). The GO controls a CAC of LSNRs, but BSA has disrupted the LSNRs aggregating as colloids with a lower value due to multiple NHSs tending towards a monolayer (Fig. 17b). BSA capping of LSNRs and LGT has weakened their cohesive forces, as BSA disrupts the aligned water dipoles, forming multiple NHSs with slight monodispersion (Fig. 17b and d). The values of La_2S_3, Ce_2S_3, and Tb_2S_3 intersect at 0.006 g% unlike Ho_2S_3 with stronger adherence of H_2O. The values decreased with concentration of $La_2S_3 \sim H_2O$. Additionally, Tb_2S_3 with aq-BSA increased the η values due to the half-filled electronic spins of $4f^{9e}$ causing oscillations aligning H_2O dipoles for comparatively stronger adhesion. On increasing Ho_2S_3, g% with aq-BSA did not produce a higher η value unlike Tb_2S_3 at 0.006 and 0.010 g% due to $4f^{9e}$, as an unpaired electron does not align the H_2O in light of the NHS of BSA (Tables S6.3 and S6.4, ESI†). The BSA monodispersion with increasing LSNR g% develops LSNR $\sim$ PB interactions on solvent adherence (Fig. S1.2, ESI†). LSNRs align the surface charges of BSA to develop multiple NHSs, resulting in a weaker NHS on a continuously flickering H_2O. The ordered trends for values for aq-LGT-BSA compared to aq-BSA alone and aq-LSNR-BSA redistributes and realigns the surface charges with concentration. The aq-BSA regularly adheres to LSNRs with increasing g% on engaging a solvent. Amounts of 0.002 g% for La_2S_3 and Ce_2S_3 produced almost the same values unlike the situation at 0.010 g%. The values of La_2S_3:GO-BSA, Ce_2S_3:GO-BSA, Tb_2S_3:GO-BSA and Ho_2S_3:GO-BSA depend on g% (Tables S6.3 and S6.4, ESI†). The trend in polynomial η for La_2S_3, Ce_2S_3 and Tb_2S_3 on increasing g% at constant temperature predicts saturation at 0.006 g% (Fig. S1.2a, ESI†). Aq-Ho_2S_3 mildly increased the η values, unlike the case at 0.006 g% due to hydrated LSNRs as the Ho_2S_3 nanorods could have aligned H_2O dipoles (Fig. S1.2b, ESI†). Increasing Ho_2S_3 g% has mildly realigned a saturated H_2O with stronger adherence, but decreases the η values due to energetically disrupting the aligned NHSs (Fig. 5b). The residual charges align the LSNR–H_2O interface with $G_{net} = G_{H_2O–H_2O} \neq G_{interfacial}$ as a polynomial relation. Thus, increasing the g% of Ho_2S_3 disrupts the NHS, which affects both the adhesive and cohesive force. Ho_2S_3 does not disrupt the H_2O and is salted out, requiring sonication to remain suspended. La_2S_3, Ce_2S_3, and Tb_2S_3 decreased the η values by weakly disrupting the adhering NHS that distinguished the $G_{H_2O–H_2O}$ and $G_{interfacial}$ on sonication. LGT realigns H_2O to enhance aq-LSNR solubility with higher η values due to effective adherence increasing τ. The rheology of aq-Ln_2S_3 with increasing temperature equalizes with their oscillation with certain ψ equipartition of the energy. The adherence of H_2O to Ln_2S_3 is equal, however, at lower temperature and the viscosity values differ due to different oscillations and ψs. The shift from Ln_2S_3 to Ln_2S_3:GO at 298.15 K, indicates GO doping reducing energy equipartition (Fig. 17). However, BSA with Ln_2S_3 and Ln_2S_3:GO have indistinguishable viscosities due to an equal adherence pattern. Robust oscillations of electron

clouds of GO with LGT influence adherence *via* ψ_s (Fig. 17a and b). Interactions of Ln_2S_3 and Ln_2S_3:GO with BSA *via* NHS have sandwiched Ln_2S_3:GO with BSA together as incompressible, that lowers the η with increasing temperature. The η of packed LSNR-BSA and LGT-BSA support expeditious resonating energy transfer for equipartition, where no energy-deficient sites are generated by varying the temperature.

    Due to its salt bridges and electrostatic sites, BSA is closely packed in between the cages or NHSs of LSNRs and LGT, lowering the η values equally (Fig. 17c and d). Tb_2S_3-BSA and Ho_2S_3-BSA interactions are weakened at 0.006 and 0.010 g% compared to Tb_2S_3 and Ho_2S_3 alone, as $4f^{\#e} \sim$ PB linkages and stronger electrostatic sites of BSA affect NHS alignment (Fig. S1.2c and d, ESI†). The η values of BSA with LGT are increased on strengthening the FE of GO and electrostatic interactions of BSA that are more soluble with LGT than LSNRs, as no FE networking exists with the LSNRs on disruption of HB. The LGT-BSA biotemplate increased BSA solubility, due to expeditious charge equalization through $4f^{\#e} \sim$ FE interfaces *via* FRET increasing the η values (Fig. S1.2d, ESI†).

4.3. Surface tension (γ, mN m^{-1})

Disruption of H_2O adhering to LSNRs and LGT alone and with BSA affect the cohesive force of the medium. The γ elaborates the structural interaction with the solvent and pdn indicates the cohesive force, and γ is calculated with pdn and density values (Tables 8, 9 and Table S1.1, ESI†) as:

$$\gamma = \left(\frac{n^0}{n}\right)\left(\frac{\rho}{\rho^0}\right)\gamma^0 \qquad (4)$$

where γ^0, n^0, ρ^0 and γ, n, ρ are the surface tension, pdn, and density of water and solution, respectively. The surface tension of aq-LGT with BSA is higher than aq-LSNR with BSA, aligning multiple NHSs with stronger cohesive forces (Tables 8, 9 and Fig. 18). LGT developed a critical aggregation temperature (CAT) at 298.15 K similar to a critical solution temperature.[47] The H_2O dipoles cap LGT to transfer a resonating energy with a moderate VWF (Fig. 18b). The CAT is controlled by $4f^{\#e}$, as GO sheets adhere to LSNRs *via* NHSs that equalise the surface energy (SE). The FE with SE of LSNRs exchange their oscillations. Aq-LSNR does not favour CAT; thus, the $4f^{\#e} \sim$ FE works to develop multiple linkages to develop CAT at $\sim$298.15 K (Fig. 18a and b). The GO wrapped the LGT and a CAT could not distinguish an SE while neither the LSNRs nor LGT produce a CAT with BSA. BSA increasing time binds the LSNRs *via* NHSs with different surface charges and heat capacities around LSNRs *via* cohad. On partially engaging the cohesive and adhesive forces expressed as cohad. BSA having higher SE and a lower γ with aq-LGT developed a critical micelle temperature (CMT) at 298.15 K (Fig. 18d). BSA did not initiate a CMT due to its PB salt bridges, and electrostatic dipoles that stabilize the SE of LGT at 298.15 K. The SEs of GO and BSA both mutually adhere at 298.15 K with the highly sensitive surfaces for expeditious energy transfer *via* VWF. The trend of change in γ values unlike the η values depicts an adherence of NHS around a core of LSNRs. The cohad infers a balances in the
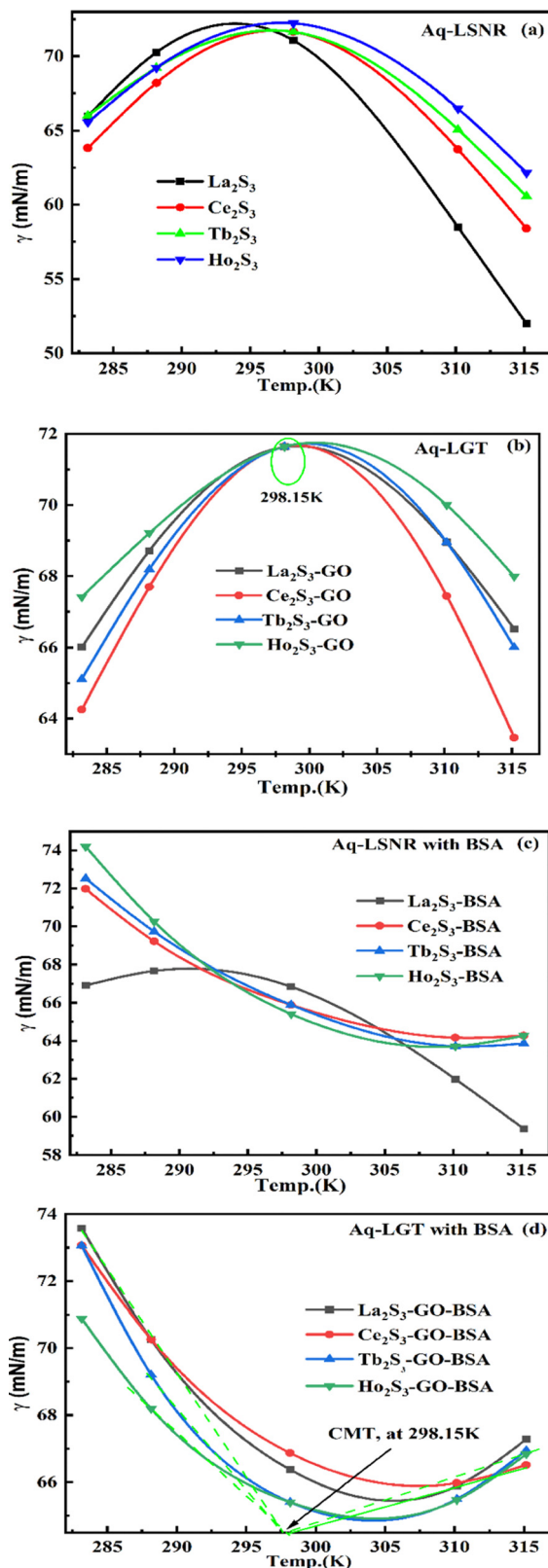
Fig. 18 Surface tension of aq-LSNR and aq-LGT with BSA at ST.

cohesive and adhesive forces of the solvent as well as the LSNR and LGT for the thermodynamic and kinetic stabilities of their

aqueous solutions preventing their coagulation (Fig. 18). The η, γ, and σ indicating aq-Ho$_2$S$_3$ with three unpaired electrons are more sensitive than other LSNRs due to the same contraction effect with stable dipoles (Fig. S1.3a, ESI†). Surfaces of LSNRs are capped with GO in manifold layers to attract the electrostatic centres of PB. LSNR:GO-BSA strengthens the electrostatic interactions with dipolar water. The lower γ values for aq-Tb$_2$S$_3$ indicate stronger adherence with LGT and BSA with a higher (Fig. S1.3d, ESI†). The 4f$^{\#e}$ engage the FE to get solvated or NHSs with increasing, and LSNR:GO with BSA further increases the adherence with increasing. The 4f$^{\#e} \sim$ FE photonic interfaces of LGT with BSA could store energy through aligned dipoles[45] by preventing the recombination of holes. The electrostatic linkages with 4f$^{\#e} \sim$ FE could develop the functional interface with a protein of specific charge with highly stabilized dipoles from 285 to 297 K; the γ value saturates but increasing H$_2$O drastically develops an NHS.

4.4. Friccohesity (σ, S cm^{-1})

HB disruption aligns H$_2$O around LSNRs and LGT separately and with BSA develops specific adherence with the cohesive force that supplements the respective FRET to E_a. It equalizes a stabilizing energy to develop σ, calculated from pdn and vft (Tables S1.1 and S1.2, ESI†):

$$\sigma = \sigma^0\left(\frac{t}{t_0} \pm \frac{B}{t}\right)\left(\frac{n}{n_0} \pm 0.0012(1-\rho)\right),$$
$$\sigma = \sigma^0\left(\frac{t}{t_0}\right)\left(\frac{n}{n_0}\right) \text{ and } \sigma = \frac{\sigma^0}{t_0 n_0}(t \times n) \quad (5)$$

where σ and σ_0 are the friccohesity of solution and solvent, respectively, $\pm B/t$ are kinetic and $\pm 0.0012(1-\rho)$ buoyancy corrections, other symbols are as usual. Corrections of the order of 1×10^{-7} are omitted. The common physicochemical parameters of solvents are rationalized as a Mansingh constant (M_c) that finds an interface between adhesive and cohesive forces. M_c depicts a mutual shear stress and the SE coefficient of a solvent for GO, LSNRs and LGT with BSA calculated with eqn (6):

$$M_c = \frac{\sigma^0}{t_0 n_0} \quad (6)$$

M_c as a quantizing coordinate of aligned H$_2$O dipoles with LSNRs, LGT and BSA indicates homogenization with equipartition of their energies with a solvent via FRET. The M_c operator transforms cohesive to oscillating energies through a mutual electrostatic reorientation of solvent molecules around the LSNRs and LGT. The friccohesity of aq-LSNR, and LGT alone and with BSA indicate spontaneous solvent adherence (Tables 10, 11 and Fig. 20). The 4f$^{\#e} \sim$ FE interfaces of LSNRs, LGT and BSA are accessible to the internal salt bridges and electrostatic dipolar linkages of BSA to attract H$_2$O dipoles. The H$_2$O dipole interacts with each constituent of LSNRs, LGT and BSA via quantized negative and positive holes to adhere H$_2$O. It avoids nanoclusters to promote PCR and SCR activities. Friccohesity generates several NHSs with different charges on surfaces that initiate the
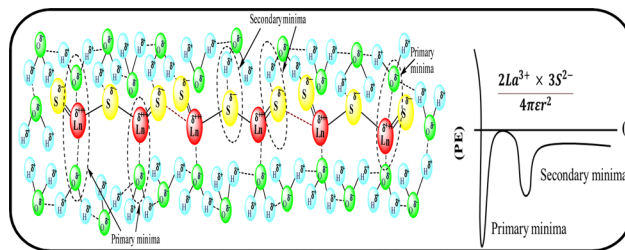
Fig. 19 Primary and secondary minima via 4f$^{\#e} \sim$ H$_2$O.

secondary global energy minima, stabilizing their NHSs for the required cohesive force. The friccohesity illustrates a mechanism and pattern of primary and secondary minima as the LSNRs, LGT and BSA interact differently through the NHS. Their NHSs mutually equalize the energy of a medium (Fig. 20).

Secondary minima attained via LSNR $\sim$ HS, LGT $\sim$ HS, and BSA $\sim$ HS interactions facilitate a FRET for mutual homogenization. The friccohesity for partitioning the secondary quantization of cohesive forces was transformed into oscillatory energy by reducing the QEB of an NHS (Fig. 19). The σ represents the CMT of LSNRs and LGT with BSA at 295 and 302.5 K, respectively, aligning the FEs at 302.5 K compared to η. It depicts a higher resolution incorporating the role of each constituent for NHS quantization (Fig. 20a and d). The σ values illustrate the reengineering of interactions to analyse a contribution from each charge to operate on the air–liquid interface at laminar-to-laminar flow. Friccohesity scans consolidate the contribution of surface energy from each laminar layer, causing a frictional force on maximum adherence with the least and higher η. Friccohesity decreases on increasing 4f$^{\#e}$ from La$_2$S$_3$ to Ho$_2$S$_3$ at 283.15 and 315.15 K unlike that at 298.15 K that expeditiously exchanges via FRET, establishing a continuity to mutually exchange the alignment of H$_2$O between adhesive and cohesive forces (Fig. 20a). LGT slightly tunes LSNR activities except for Ho$_2$S$_3$ with higher and the least SE. The ψ_{PE} compensates for the electronic cloud of ψ_{UPE} with the vibrant activities of FE (Fig. 20b). Friccohesity indicates LSNR and LGT systematisation on BSA capping unlike the and values with cohad on mutually equilibrating the binding and dispersing forces, respectively. The LSNRs and LGT both indicate CMT with BSA where the friccohesity mutual resonating energies transfer to normalise the cohad, the ratio of the cohesive and adhesive forces (Fig. 20c and d).

4.5. Friccohesity velocity (σ_v, cm s^{-1})

The disruption of LSNRs, GO, and LGT alone and with BSA causes reorientation with a certain velocity that could be decisive with respect to their adhesive and cohesive forces to mutual stabilization. The solvent molecules adhere around LSNRs and LGT surfaces, forming an NHS and to suspend them needs a strengthening of the structural framework with the required adhesion supported by mutual cohesion. The spontaneity of a template with respective ψ_s establishes a close continuity as an ordered state. Locally aligning and adhering a solvent induce collisions for continuous flow oscillation to maintain
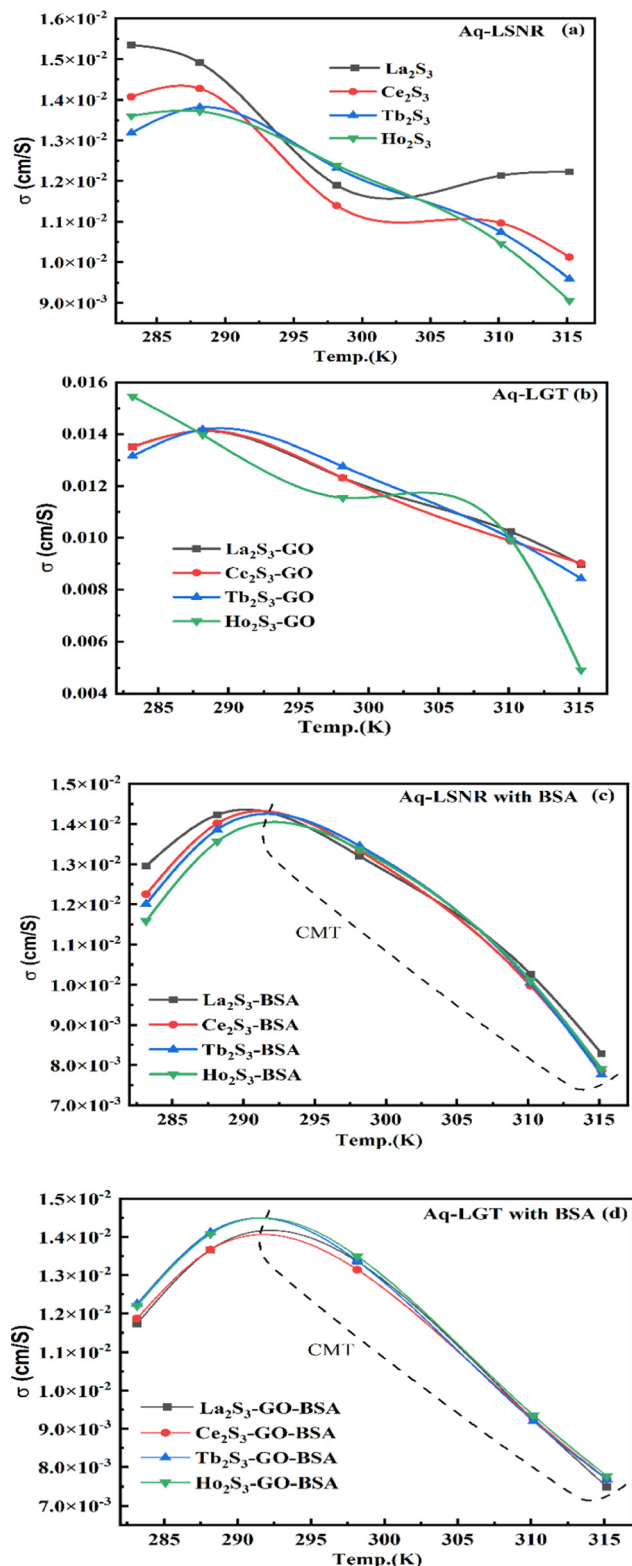
Fig. 20 Friccohesity of aq-LSNR and aq-LGT with BSA at 5 T.

cohesion, so σ_v is calculated with σ values (Tables 10 and 11).

$$\text{Friccohesity velocity } (\sigma_v) = \frac{1}{\sigma \text{ s cm}^{-1}}, \text{ or } \sigma_v \text{ cm s}^{-1} \qquad (7)$$

The σ_v values of LSNRs and LGT separately and with BSA at constant pH and temperature indicate alignment in capillary flow (Tables S5.9 and S6.0). The reorienting chemical species could initiate a solvent-disrupting activity to dislocate a free hydrogen-bonded state and adhere to LSNRs, GO, and LGT with specific velocity. Adhered H_2O spontaneously align on the outer surface of the NHS, initiating the development of solvent–solvent coherence. The σ_v depicted as adherence and coherence move dynamically.

4.6. Isentropic compressibility ($K_{S,\phi}$)

LSNRs, GO, LGT, and BSA reorient to adhere H_2O from the hydrogen-bonded state with a higher cohesive force, causing monodispersion. Thereby charge expression plays a key role in generating entropy on reorienting and aligning them. $K_{S,\phi}$ indicates constant entropy during these activities as the species maintain their structures, except for infinitesimal changes in friccohesity, for initiating interactions producing $K_{S,\phi}$ in the 5×10^{-7} cm s^2 g^{-1} range (Tables S7.5 and S7.6, ESI†). $K_{S,\phi}$ is calculated using density and sound velocity (Tables S1.3, S1.8 and S8.2, ESI†):

$$K_{s,\phi} = \frac{1}{u^2 \rho} \qquad (8)$$

where u and ρ are sound velocity and density of solution. The $K_{S,\phi}$ of LSNRs and LGT alone and with BSA depict their electrostatic interaction with almost constant entropy due to the ordered alignment maintained by adherence and coherence within infinitesimal changes (Tables S7.5 and S7.6, ESI†). The $K_{S,\phi}$ of LSNRs and LGT gradually decrease with increasing temperature as it disrupts the ordered state. At higher temperature the ρ values are lower, as cohesive forces are weakened by oscillation of their binding energy. At lower temperature, a mild oscillation indicates a maximum $K_{S,\phi}$ but increasing temperature has weakened the ε of LSNRs and LGT with BSA (Fig. S1.5 and S1.6, ESI†). The increasing temperature indicates stronger LGT $\sim$ BSA interaction with $4f^{\#e} \sim$ FE $\sim$ PB linkages due to the lowest friccohesity, as adherence is dominated by the cohesive forces of a uniform NHS.

5. Thermodynamics for PCPs, PCR and SCR activities

5.1. E_a, kJ mol^{-1}

LSNR and LGT dissolution need energy and space to disperse in H_2O, so the HB disruption by weakening cohesive forces activates H_2O alignment around them via electrostatic and ionic dipoles. LSNR and LGT dispersion acquire energy from water directly, indicating their interacting nature with a certain state function. The Ln^{3+} and S^{2-} of LSNRs vis-à-vis the skeletal edges of GO and their spatial occupation of the LGT interface encounter BSA with an active electronic cloud. These respond to

interlinking of oscillations and thermal energies on increasing temperature as:

$$\frac{p^2}{2m} = \frac{1}{2\pi}\sqrt{\frac{k}{\mu}} \qquad (9)$$

The acquired energy does not break bonds, but rather activates a whole structure to develop ψ that resonates energy to participate in interactions. E_a is calculated with eqn (9) and $\log \eta$ *vs.* $(1/T)$ and $\log(abs)$ *vs.* $(1/C_t)$ are plotted (Tables S1.4–S2.1, ESI†), where T is temperature and C_t is dye degradation concentration, with time t min fitted as shown below:

$$\log(\eta) = \log A - \frac{E_a}{R} \times \left(\frac{1}{T}\right), \text{ or slope} = -\frac{E_a}{2.303 \times R}, \qquad (10)$$

$$E_a = -\text{slope} \times 2.303 \times R$$

E_a is calculated with dye degradation concentration (C_t) on PCR and SCR.

$$\log(abs) = \log A - \frac{E_a}{R} \times \left(\frac{1}{C_t}\right), \text{ or slope} = -\frac{E_a}{2.303 \times R}, \qquad (11)$$

$$E_a = -\text{slope} \times 2.303 \times R$$

$E_a > 0$ for Ln_2S_3 and Ln_2S_3:GO indicates HB disruption realigning and reorienting H_2O to flow in a streamlined way within a uniform capillary. $(E_{a,LSNR} > E_{a,LGT}) > 0$ indicates higher activities of the FE despite it getting doped with LSNRs. Thus, the $4f^{\#e}$ of LGT resonates energy to transfer to the closest FE to photocatalyze dyes in a shorter time and is proven to be an efficient photocatalyst to induce FRET. E_a calculated with PCR is 10 times higher than with PCP, as multiple and manifold collisions of $4f^{\#e} \sim$ FE utilize their energies to align (Fig. 21 and Tables S1.4–S2.1, ESI†) compared to shear stress being used to align.

5.2. Thermodynamic parameters ΔH, ΔG, and ΔS

Thermodynamic functions define the interacting activities of LSNRs, GO, LGT, and BSA in aqueous solution as state functions ΔH, ΔG, and ΔS calculated from E_a (Tables S1.4–S2.1, ESI†):

$$\Delta H = E_a - 2.303RT \text{ or } \Delta H = E_a - 2.303RC_t \qquad (12)$$

$$\Delta G = 2.303RT \log(abs) \text{ or } \Delta G = 2.303RC_t \log(abs) \qquad (13)$$

$$\Delta S = \frac{(\Delta H - \Delta G)}{T} \text{ or } \Delta S = \frac{(\Delta H - \Delta G)}{C_t} \qquad (14)$$

$\Delta G < 0$, $\Delta H < 0$ and $\Delta S > 0$ with LSNRs indicate spontaneously exothermic disordered interaction activities, reducing dyes in a longer time (Tables S1.4–S2.1, ESI†). $\Delta H < 0$, $\Delta G > 0$ and $\Delta S < 0$ indicate an aligned LGT with H_2O dipoles where non-spontaneous endothermic activity has reduced the dyes in shorter time, acquiring a lower E_a (Tables S8.3–S8.6, ESI†). The aligned and ordered LGT with $\Delta G > 0$ has a stronger dipolar system ($\Delta S < 0$), as the $h\nu$ absorption ability is rapid for the PCR and SCR of dyes (Tables S4.2–S5.9, ESI†). Sonication disrupts the NHS and the secondary bonds release energy,
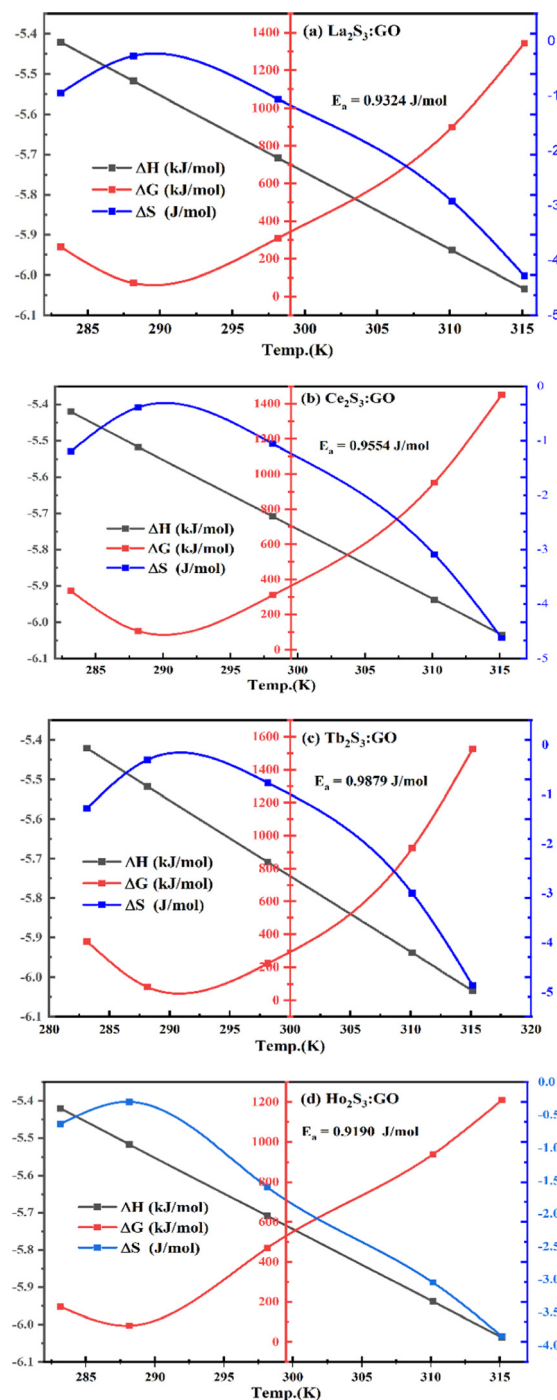
Fig. 21 The thermodynamic parameters with increasing temperature of Aq-LGT for PCR.

increasing the overall heat content as an exothermic process. E_a for LGT is the lowest, as the FE and $4f^{\#e}$ are both pre-activated with a least QEB of $4f^{\#e}$ and ordered FE, as $\langle\psi_{4f^{\#e}}|\psi_{FE}^2\rangle$ is a normalized quantum string on the surface. With a mutual contribution, the RE of FGs and $4f^{\#e}$ are partially shed to reorient and align GO around LSNRs is favoured by NHS mutually (Fig. 5b). LSNRs and LGT could not affect E_a with BSA, despite having many amino acids, tryptophan, salt bridges, and electrostatic linkages with H_2O dipoles due

to their structural integrity. Tb_2S_3 with $4f^9$ strongly aligns the H_2O around BSA.

6. Photocatalytic reduction (PCR) of MB, MO, BBR and BBG under sunlight

The $h\nu$ could interact with the electronic cloud available on the surfaces of LSNRs and LGT as an excessive cohesive force with maximum electronic sites to receive photons. Additionally, the packing of LSNRs, LGT, and GO photocatalyst causes a higher increasing rate of PCR. The monodispersion of photocatalyst generates a lower surface area with a maximum number of $h\nu$ receiving sites. Therefore, the study of PCPs is noted as an essential prerequisite for monodispersion and to have thermodynamic and kinetic stability for the efficient use of active site of LSNR, GO, and LGT photocatalysts. Thus, the PCPs have been considered as preparatory ground for PCR and SCR. Fig. 22 depicts the homogeneous to heterogeneous phase; initially it dispersed in aqueous solution and after 90 min it was settled at the bottom, as these did not engage the dipoles of water without monodispersion. Thus, an adequate adherence of H_2O is necessary for monodispersion for reusability, as the photon could not weaken the cohesive force for adhering H_2O molecules, denoted as the secondary cohesive force. The primary cohesive forces do not monodisperse the sample and the secondary cohesive forces generate functional sites to enhance increasing rate of PCR and SCR activities. LSNRs and LGT both oscillate the electronic cloud to gain an electronic charge of dyes having quaternary nitrogen (QN) with electron-deficient sites through FRET. LSNRs and LGT both resonate their respective electronic charges to overcome the QEB to approach cycles. Their resonating energies counterbalance the respective residual charge without balancing the holes. GO holes out of hexagonal GO sheets PCR the MB, MO, BBR, and BBG with LGT. GO with a high mobility of charge carriers gains higher thermal conductivity to capture a maximum number of $h\nu$.[20,35] LGT has reduced dyes in ~ 30–90 min and GO in ~ 120 min with Φ of 99–100 and 87%, respectively.[3] The @PCR and @SCR for dyes are calculated as:

$$@PCR/SCR\% = \frac{C_0 - C_t}{C_0} \times 100 \qquad (15)$$
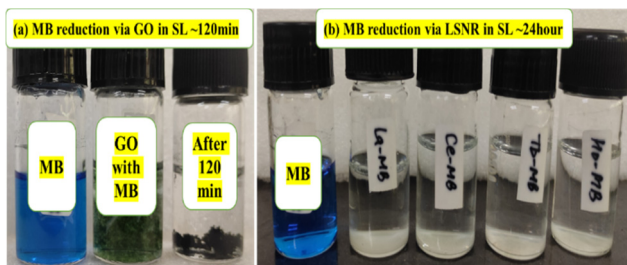
Fig. 22 PCR of MB: (a) aq-GO (b) aq-LSNR under SL in 120 min and 24 h, respectively.

Fig. 23 PCR of dyes under SL with LGT ~ 30–90 min.

C_0 is the initial dye concentration at time $t = 0$, and C_t is the concentration of reduced dye at t min. UV/Vis absorbance has been used to calculate the quantum yield using Einstein eqn (16):

$$E = mc^2 \qquad (16)$$

$$abs = \varepsilon l c, \ \Delta c = \frac{\Delta Abs}{\varepsilon l} \qquad (17)$$

$$n_a = \frac{E_a}{h}, \ n_e = \frac{E_e}{h}, \ \Phi = \frac{n_e}{n_a} \qquad (18)$$

where m is the mass derived from eqn (17) with Δc the change in concentration, ΔAbs is the change in absorbance, c is the speed of a photon (3×10^8 m s^{-1}) and E_a is the absorbed energy and E_e the emitted energy, n_a is the number of photons absorbed and n_e is the number of photons emitted. The $h\nu$ from sunlight generated phonons different frequencies, so a particular energy is used to calculate the number of $h\nu$. Absorption is used to calculate C_t, which directly depends on number of $h\nu$, which is then used to calculate n_a and n_e (Fig. 24).

LGT has reduced BBG, BBR, MB and MO with 90–100, 87–97, 90–96, and 93–95% @PCR and with 94–100, 94–99, 93–97, and 93–95% Φ, respectively due to their different structures (Tables S8.3.0–S8.6, ESI†) Tb_2S_3:GO and Ho_2S_3:GO are effective
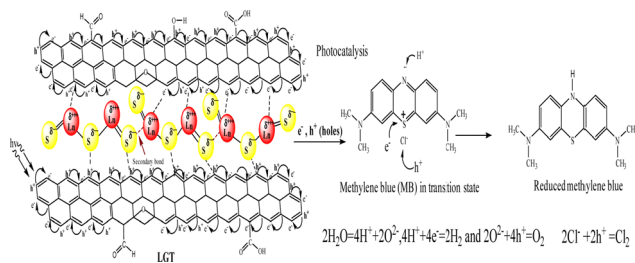
Fig. 24 LGT electronic hole generation for the PCR of dyes.

Fig. 25 Photocatalysis of (a) BBR, (b) BBG, (c) MB and (d) MO through LGT.

photocatalysts with $4f^{9e}$ and $4f^{11e}$, respectively. Photocatalysts and dyes both align mutually to exchange their electronic charges as ψ overcomes the QEB. MB with $4-CH_3$ causes and ER effect on absorbing $h\nu$ (Fig. 25c). The active sites of dyes interact with LSNRs and LGT, but QN receives electron holes from LSNRs and LGT through FRET (Fig. 25a). LSNRs and LGT distinguished the azo group of MO despite resistance to the conjugation of electrons (Fig. 25d). MO dye is reduced in a longer time than BBG, BBR, or MB as the hydrophobicity of $-CH_3$ influences the delocalisation of the π electrons. The binding constant (k_b) of MO with LSNRs and LGT is higher with a lower reduction, indicating oscillation of MO to interact with the photocatalysts. The higher k_b blocks the $h\nu$ receiving sites of the photocatalysts, inducing defects on interacting with them as well as with dyes. The $-N=N-$ azo and $Na^+-SO_3^-$ interact, reducing the surface area to become settled at the bottom; therefore, the PCPs and PCR are directly interfaced. ERG ($-CH_3$) intensifies their holes for reducing BBG and BBR in a shorter time than MO with LGT and LSNRs, initiating an ROC via $h\nu$. The QNs of BBG and BBR received the e^- holes from LGT via ψ for the PCR (Fig. 25c and d). BBR, BBG, MB, and MO are reduced at λ_{max} of 550, 585, 665, and 465 nm, respectively, with UV/vis, light and sunlight for disposal. The reduced dyes were phased out from wastewater for recycling (Fig. 23). The $h\nu$ weakened the shared electron and FGs accompanied by certain thermodynamic parameters. $\Delta H < 0$, $\Delta G > 0$ and $\Delta S < 0$ as an exothermically spontaneous reaction has fixed the @PCR and @SCR of dyes. The $h\nu$ have struck FE and $4f^{\#e}$ on decreasing S compared to aq-LSNR to minimize the collision of holes.

The absorbance of wastewater effluents decreases with the 4f electrons of the photocatalyzing properties of the photocatalyst. An 87–100% reduction of dyes was observed after $\sim$60 min. The enhanced photocatalyzing performance of LGT was noticed due to a higher amount of UV light being detained and higher photon trapping ability. The catalysing activities were observed by plotting (C_{4fe}/C_0) vs. $4f^{\#e}$, to observe the role of electronic activities during PCR (Fig. 26). The @$4f^{\#e}$ of the photocatalyst indicates the excellent photocatalyzing ability extended to determine the role of the maximum number of 4f electron in the lanthanide series.

6.1. Reusability of LGT photocatalyst

The reusability of a photocatalyst is studied by using the same photocatalyst over 4 to 5 cycles to reduce the fresh effluents. Every cycle reduced the active sites of the photocatalyst, as the quantum yield of the dyes decreases with successive cycles. PCR performance has not significantly decreased after 4–5 cycles
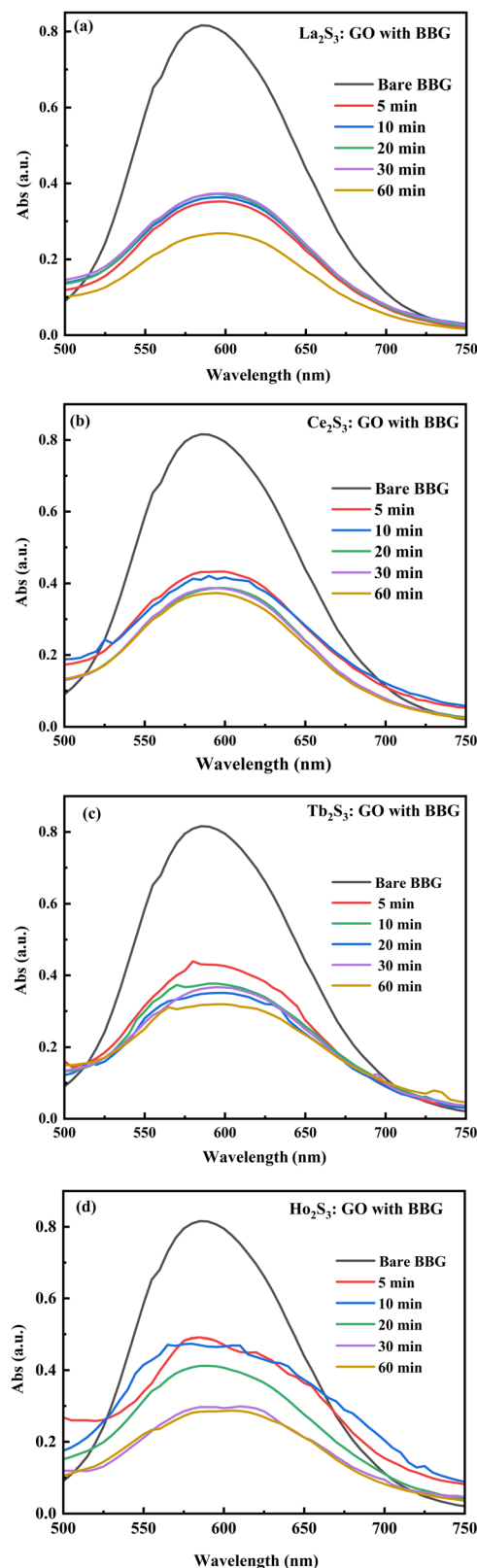
shorter time. Additionally, the MB due to two different ethyl groups with an almost nil effect of ERGs could not develop an intensified DOS and has taken more time for reduction than BBR or BBG (Fig. 22).

7. Sonocatalytic reduction (SCR) of MB, MO, BBR and BBG

LSNRs, GO, and LGT were not homogeneously dissolved in water and phased out without electrostatically engaging the dipoles of water to transfer a cohesive force as PE to oscillatory energy. The $h\nu$ was not captured by photocatalysts which were sonicated for monodispersion to SCR the dyes by generating functional sites. The sonication generates localized energy centres denoted as charge cavitation. The charge cavitation gains a higher surface area and available electronic oscillatory or resonating activity to develop ψ that cross over a QEB of electronic charge sites of dyes, and the species remained monodispersed. The sonication was further extended from monodispersion to generate photonic waves with a certain $h\nu$, equally capable of reducing dyes. Therefore, in both PCR and SCR, a monodispersion of photocatalyst and dyes is a prerequisite. Therefore, the PCPs as a database predict thermodynamic and kinetically stable states for receiving $h\nu$ to generate ROC. SCR was conducted to equate PCR efficiency with monodispersion and then the $h\nu$ was supplied and sonication continued to SCR. Sonication weakened the PE of shared electrons and FGs with both oscillating as charged clouds on a cavitation that aligns the electronic cloud shifting to a higher energy state to generate e^- and h^+ holes. The sonication induces mechanical energy to generate an electron-rich domain e^- or electronic-charge-deficient h^+ holes. LGT, LSNRs and GO solutions with dyes dissociated their bonds to move the electrons towards the respective holes of dyes for SCR.[48] Sonication could also break the bonds and release energy due to oscillations.[39] $\Delta S < 0$ and $\Delta S > 0$ indicate ordered and disordered configurations, and oscillations of LGT might be mildly disordered on aligning dyes with 40–90% Φ (Tables S7.7–S8.0, ESI†). The SCR route is effective for dipolar LSNRs and LGT by sonicating at 28 KHz for 5, 10, 20, 30, and 60 min, consequently raising the temperature to 298.15, 301.15, 305.15, 308.15, and 313.15 K, respectively. SCR structurally

reduces a dye as a sono-frequency attacks the π-conjugation to enhance the electronic charge density. The structurally damaged dye does not respond to environmental and biological processes. A highly oxidised structure with $\Delta S < 0$ is phased out (Tables S4.2–S5.8, ESI†). $\Delta G > 0$ indicates interaction between dyes and LGT on sonication. E_a is not needed for
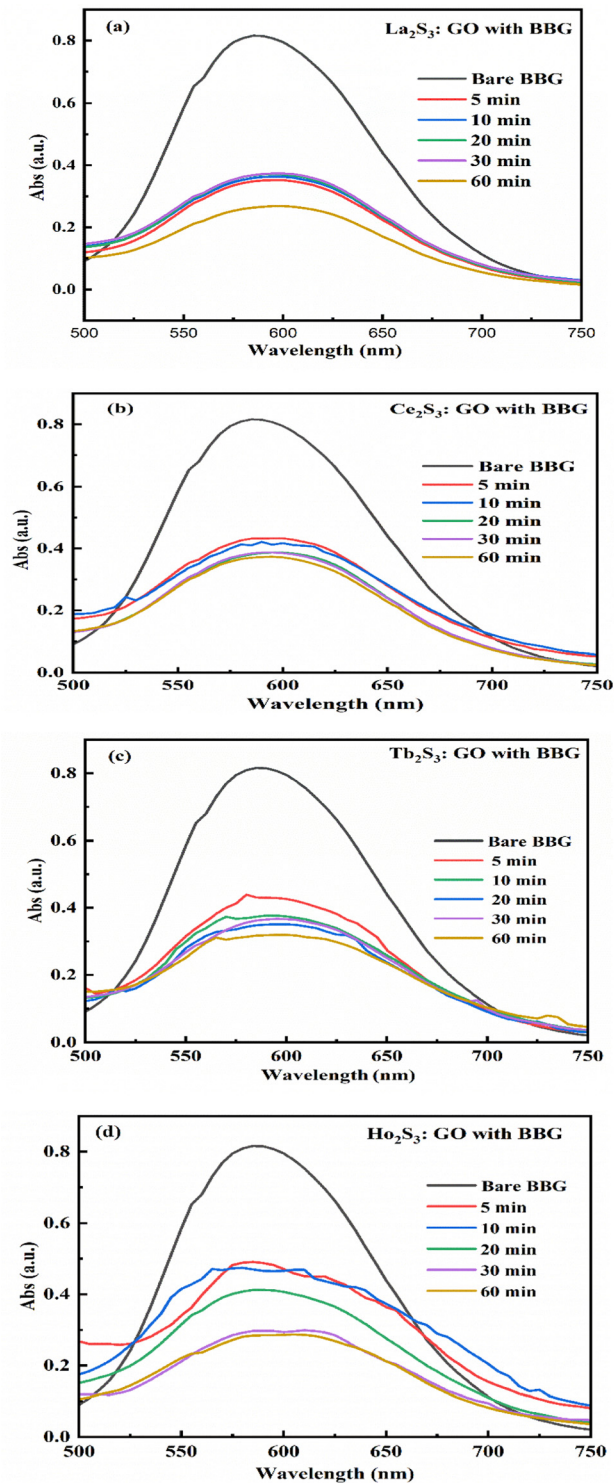

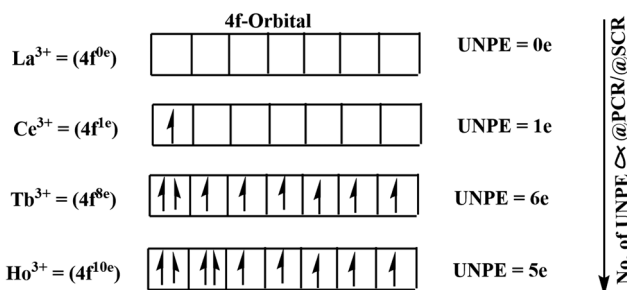Fig. 30 SCR of BBG with LGT and other dyes given (Fig. S8–S11, ESI†).

Fig. 29 The number of unpaired electrons directly enhances the @PCR and @SCR.

8. Tables

Table 5 Dynamic light scattering analysis of GO, LSNRs and LGT aqueous solution

Parameter	GO	La$_2$S$_3$	La$_2$S$_3$:GO	Ce$_2$S$_3$	Ce$_2$S$_3$:GO	Tb$_2$S$_3$	Tb$_2$S$_3$:GO	Ho$_2$S$_3$	Ho$_2$S$_3$:GO
PDI	—	0.425	1.591	1.002	0.175	0.619	1.023	5.35	1.369
Diameter (nm)	6.10	457.0	307	17.66	263.7	486	212.9	16.57	325
	—	230.3	—	—	109.3	—	97.60	—	157.7
Volume (%)	100	74.8	100	100	47.2	100	52.1	100	20.9
	—	25.2	—	—	52.8	—	47.9	—	79.1
Width	2.32	344.00	158.70	9.28	161.10	169.30	126.80	6.18	98.00
	—	54.90	—	—	44.40	—	36.50	—	104.30
Mobility (μ s^{-1})	0.81	1.74	−0.04	−0.04	1.22	0.30	−1.40	0.62	0.87
Zeta pot. (mV)	10.41	22.24	−0.49	−0.51	15.64	3.88	−17.60	7.97	11.08
Charge (fC)	0.00052	0.327	−0.004	−0.0064	0.033	0.036	−0.057	0.059	0.032
Polarity	+ve	+ve	−ve	−ve	+ve	+ve	−ve	+ve	+ve
Conductivity (μs cm^{-1})	50	43	18	27	17	24	20	38	22

Table 6 Viscosities (mPa S) of LSNRs and LGT

Temp. (K)	La$_2$S$_3$	Ce$_2$S$_3$	Tb$_2$S$_3$	Ho$_2$S$_3$	La$_2$S$_3$:GO	Ce$_2$S$_3$:GO	Tb$_2$S$_3$:GO	Ho$_2$S$_3$:GO
283.15	1.0152	0.9035	0.8705	0.8514	0.8944	0.8680	0.8596	0.9281
288.15	1.0475	0.9736	0.9565	0.9497	0.9704	0.9565	0.9668	0.9668
298.15	0.8746	0.8787	0.8827	0.8945	0.8825	0.8827	0.9142	0.8275
310.15	0.7095	0.6986	0.6986	0.6950	0.7058	0.6913	0.6986	0.6950
315.15	0.6379	0.5930	0.5833	0.5650	0.5990	0.5748	0.5586	0.6301

Table 7 Viscosities (mPa S) of LSNRs and LGT with BSA

Temp. (K)	BSA	La$_2$S$_3$ BSA	Ce$_2$S$_3$ BSA	Tb$_2$S$_3$ BSA	Ho$_2$S$_3$ BSA	La$_2$S$_3$:GO BSA	Ce$_2$S$_3$GO BSA	Tb$_2$S$_3$:GO BSA	Ho$_2$S$_3$:GO BSA
283.15	0.8699	0.8668	0.8837	0.8727	0.8617	0.8638	0.8699	0.8973	0.8669
288.15	0.9634	0.9630	0.9702	0.9668	0.9531	0.9599	0.9600	0.9770	0.9599
298.15	0.8827	0.8824	0.8788	0.8866	0.8748	0.8866	0.8788	0.8747	0.8826
310.15	0.6367	0.6364	0.6403	0.6402	0.6439	0.6465	0.6474	0.6437	0.6543
315.15	0.4945	0.4937	0.5067	0.4977	0.5099	0.5054	0.5128	0.5157	0.5209

Table 8 Surface tension (mN m^{-1}) of LSNRs and LGT

Temp. (K)	La$_2$S$_3$	Ce$_2$S$_3$	Tb$_2$S$_3$	Ho$_2$S$_3$	La$_2$S$_3$:GO	Ce$_2$S$_3$:GO	Tb$_2$S$_3$:GO	Ho$_2$S$_3$:GO
283.15	65.97	63.82	66.01	65.56	66.01	64.25	65.11	67.41
288.15	70.25	68.19	69.21	69.21	68.72	67.70	68.19	69.21
298.15	71.06	71.64	71.64	72.22	71.63	71.64	71.64	71.64
310.15	58.481	63.725	65.07	66.48	68.95	67.44	68.95	70.00
315.15	51.98	58.38	60.56	62.15	66.52	63.47	66.01	67.99

Table 9 Surface tension (mN m^{-1}) of LSNRs and LGT with BSA

Temp. (K)	BSA	La$_2$S$_3$ BSA	Ce$_2$S$_3$ BSA	Tb$_2$S$_3$ BSA	Ho$_2$S$_3$ BSA	La$_2$S$_3$:GO BSA	Ce$_2$S$_3$:GO BSA	Tb$_2$S$_3$:GO BSA	Ho$_2$S$_3$:GO BSA
283.15	74.21	66.91	71.97	72.52	74.20	73.58	73.07	73.06	70.88
288.15	70.799	67.67	69.21	69.73	70.26	70.26	70.26	69.21	68.19
298.15	66.868	66.84	65.89	65.89	65.41	66.37	66.87	65.41	65.40
310.15	65.995	61.98	64.16	63.71	63.71	65.89	65.97	65.50	65.47
315.15	67.00	59.36	64.27	63.86	64.27	67.28	66.51	66.95	66.83

Table 10 Friccohesites (cm S^{-1}) of LSNRs and LGT

Temp. (K)	La$_2$S$_3$ (10^{-4})	Ce$_2$S$_3$ (10^{-4})	Tb$_2$S$_3$ (10^{-4})	Ho$_2$S$_3$ (10^{-4})	La$_2$S$_3$:GO (10^{-4})	Ce$_2$S$_3$:GO (10^{-4})	Tb$_2$S$_3$:GO (10^{-4})	Ho$_2$S$_3$:GO (10^{-4})
283.15	154	140	132	136	135	135	132	155
288.15	149	143	138	137	141	141	142	140
298.15	119	114	123	124	123	123	128	116
310.15	121	110	107	105	102	099	100	099
315.15	122	101	096	091	090	090	084	049

Table 11 Friccohesity (cm S^{-1}) of LSNRs and LGT LGT with BSA

Temp. (K)	BSA (10^{-4})	La$_2$S$_3$ (10^{-4})	Ce$_2$S$_3$ (10^{-4})	Tb$_2$S$_3$ (10^{-4})	Ho$_2$S$_3$ (10^{-4})	La$_2$S$_3$:GO (10^{-4})	Ce$_2$S$_3$:GO (10^{-4})	Tb$_2$S$_3$:GO (10^{-4})	Ho$_2$S$_3$:GO (10^{-4})
283.15	117	130	122	120	116	117	119	123	122
288.15	136	142	140	139	136	137	137	141	141
298.15	132	132	133	135	134	134	131	134	135
310.15	096	103	100	100	101	092	092	092	093
315.15	074	083	079	078	079	075	077	077	078

9. Conclusion

Multifunctional LSNR and LGT photocatalysts and adsorbents were prepared and had enhanced solubility of BSA by initiating interactions with the peptide bonds and electrostatic dipoles of aq-BSA with solubilizing activities. Physicochemical properties and thermodynamic functions of aq-LSNR, and aq-LGT alone and with 0.010 g% BSA at 283.15–315.15 K and within 0.002–0.01 g% @0.004 g% at 298.15 K indicating structural stability by doing PCR and SCR activities. The physicochemical properties and thermodynamic functions of BSA with LSNRs and LGT indicates a stronger 4f$^{\#e}$ $\sim$ FE interface with electrostatic dipoles, peptide bonds, and salt bridges as a robust approach in the area of lanthanide chemistry with biomolecules. The stronger temperature and concentration effect with structural stability, functionality, and thermal stability of LSNRs and LGT enabling their reusability for PCR and SCR activities. LSNRs with a stronger $h\nu$ trapping ability to photocatalyze the fluorescent dyes in a longer time while LGT has shortened reduction time due to 4f$^{\#e}$ $\sim$ FE interfaces. LGT recycled wastewater containing fluorescent effluents in $\sim$60 min compared to LSNRs and GO with $\sim$24 h and 120 min, respectively. LGT has reduced BBG, BBR, MB, and MO as 90–100, 87–97, 90–96, and 93–95% @PCR with 94–100, 94–99, 93–97, and 93–95% quantum yields, respectively. Each dye was sonicated @28 kHz with LSNRs and LGT separately for 5, 10, 20, 30, and 60 min were consequently raised to 298.15, 301.15, 305.15, 308.15, and 313.15 K, respectively, as an exothermic activity of LSNRs and an LGT support with thermodynamic functions. SCR has reduced the dyes with 40 to 90% Φ. PCR and SCR activities indicated that LGT is a good photocatalyst and a solubilizing agent with excellent reusability.

Abbreviations

GO	Graphene oxide
LSNRs	Lanthanide sulphide nanorods
LGT	Lanthanide GO template
MB	Methylene blue
BBR	Brilliant blue red
BBG	Brilliant blue green
MO	Methylene orange
BSA	Bovine serum albumin
PCPs	Physicochemical properties
FT-IR	Fourier transform infrared spectroscopy
GT	Graphite
GtO	Graphite oxide
RB	Round bottom flask
RPM	Revolutions per minute
aq	Aqueous
PDN	Pendant drop number
VFT	Viscous flow time
wt	Weight
SCR	Sonocatalytic reduction
FE	Functional edge
RE	Resonating energy
HHI	Hydrophilic–hydrophilic interactions
HB	Hydrogen bond
PB	Peptide bond
CAT	Critical aggregation temperature
SL	Sunlight
PCR	Photocatalytic reduction
ERG	Electron releasing group
TGA	Thermogravimetric
DTG	Differential thermal gravimetry

Author contributions

Krishan Kumar conducted the bench work, calculations, plotting figures and other designs for effective discussion and conclusive. Bhargab Sahoo initiated formulating the molecular solution preparation for accurate stoichiometry to measure the primary data of binary systems. Tara Chand Meghwal initiated formulating the molecular solution preparation for accurate stoichiometry to measure the primary data of ternary systems. Prof. Man Singh was in charge of overall supervision for

conducting the research work, frequent discussions, exploring new models outer experiment observations and matching with the explored scientific exhalations to substantially create the new science out of the research. Funding Sources There was no funding source.

Conflicts of interest

The authors confirm that there is no conflict of interest.

Acknowledgements

References

1 X. Zeng, Y. Liu, T. Zhang, J. C. Jin, J. L. Li, Q. Sun, Y. J. Ai, M. L. Feng and X. Y. Huang, Ultrafast and selective uptake of Eu3+ from aqueous solutions by two layered sulfides, *Chem. Eng. J.*, 2021, **420**, 127613.

2 R. Kumar, S. Sahoo, E. Joanni, R. K. Singh, K. Maegawa, W. K. Tan, G. Kawamura, K. K. Kar and A. Matsuda, Heteroatom doped graphene engineering for energy storage and conversion, *Mater. Today*, 2020, **39**, 47–65.

3 S. Dev and M. Singh, Metallic sulfide nanoparticles anchored graphene oxide: Synthesis, characterization and reduction of methylene blue to leuco methylene blue in aqueous mixtures, *J. Phys. Chem. Solids*, 2020, **139**, 109335.

4 A. T. Smith, A. M. LaChance, S. Zeng, B. Liu and L. Sun, Synthesis, properties, and applications of graphene oxide/reduced graphene oxide and their nanocomposites, *Nano Mater. Sci.*, 2019, **1**, 31–47.

5 K. Kumar, R. P. Dave, S. Dev and M. Singh, Study of molar properties of GO after doping with transition metals for photodegradation of fluorescent dyes, *RSC Adv.*, 2022, 29734–29756.

6 J. Dadashi, M. A. Ghasemzadeh and M. Salavati-Niasari, Recent developments in hydrogels containing copper and palladium for the catalytic reduction/degradation of organic pollutants, *RSC Adv.*, 2022, **12**, 23481–23502.

7 S. Roméro, A. Mosset, J. C. Trombe and P. Macaudière, Low-temperature process of the cubic lanthanide sesquisulfides: Remarkable stabilization of the γ-Ce2S3 phase, *J. Mater. Chem.*, 1997, **7**, 1541–1547.

8 İ. A. Kariper, Synthesis and characterization of cerium sulfide thin film, *Prog. Nat. Sci.: Mater. Int.*, 2014, **24**(6), 663–670.

9 İ. A. Kariper, The production of UV absorber amorphous cerium sulfide thin film, *Mater. Res.*, 2017, **20**, 1345–1349.

10 C. Liu, Z. Yu, D. Neff, A. Zhamu and B. Z. Jang, Graphene-based supercapacitor with an ultrahigh energy density, *Nano Lett.*, 2010, **10**, 4863–4868.

11 G. Darabdhara, M. R. Das, S. P. Singh, A. K. Rengan, S. Szunerits and R. Boukherroub, Ag and Au nanoparticles/reduced graphene oxide composite materials: Synthesis and application in diagnostics and therapeutics, *Adv. Colloid Interface Sci.*, 2019, **271**, 101991.

12 M. Ubaidullah, A. M. Al-Enizi, T. Ahamad, S. F. Shaikh, M. A. Al-Abdrabalnabi, M. S. Samdani, D. Kumar, M. A. Alam and M. Khan, Fabrication of highly porous N-doped mesoporous carbon using waste polyethylene terephthalate bottle-based MOF-5 for high performance supercapacitor, *J. Energy Storage*, 2021, **33**, 102125.

13 A. Roca-Sabio, M. Regueiro-Figueroa, D. Esteban-Gómez, A. de Blas, T. Rodríguez-Blas and C. Platas-Iglesias, Density functional dependence of molecular geometries in lanthanide(III) complexes relevant to bioanalytical and biomedical applications, *Comput. Theor. Chem.*, 2012, **999**, 93–104.

14 T. Mirkovic, E. E. Ostroumov, J. M. Anna, R. van Grondelle, Govindjee and G. D. Scholes, Light absorption and energy transfer in the antenna complexes of photosynthetic organisms, *Chem. Rev.*, 2017, **117**(2), 249–293.

15 X. Wei, H. Feng, L. Li, J. Gong, K. Jiang, S. Xue and P. K. Chu, Synthesis of tetragonal prismatic γ-In2Se3 nanostructures with predominantly {110} facets and photocatalytic degradation of tetracycline, *Appl. Catal., B*, 2020, **260**, 118218.

16 R. Tondwal and M. Singh, Chitosan functionalization with a series of sulfur-containing α-amino acids for the development of drug-binding abilities, *J. Appl. Polym. Sci.*, 2018, **135**, 1–14.

17 S. Mahapatra, G. Madras and T. N. G. Row, *Ind. Eng. Chem. Res.*, 2007, **46**, 1013–1017.

18 Z. Li, T. M. Rayder, L. Luo, J. A. Byers and C. K. Tsung, Aperture-Opening Encapsulation of a Transition Metal Catalyst in a Metal-Organic Framework for CO2 Hydrogenation, *J. Am. Chem. Soc.*, 2018, **140**, 8082–8085.

19 P. Nuengmatcha, S. Chanthai, R. Mahachai and W. C. Oh, Sonocatalytic performance of ZnO/graphene/TiO2 nanocomposite for degradation of dye pollutants (methylene blue, texbrite BAC-L, texbrite BBU-L and texbrite NFW-L) under ultrasonic irradiation, *Dyes Pigm.*, 2016, **134**, 487–497.

20 M. Sun, J. Ma, M. Zhang, Y. Xiao, Y. Zhu and S. Zhang, Thiourea-modified Fe3O4/graphene oxide nanocomposite as an efficient adsorbent for recycling Coomassie brilliant blue from aqueous solutions, *Mater. Chem. Phys.*, 2020, **241**, 122450.

21 C. M. Marin, L. Wang, J. R. Brewer, W. N. Mei and C. L. Cheung, Crystalline α-Sm2S3 nanowires: Structure and optical properties of an unusual intrinsically degenerate semiconductor, *J. Alloys Compd.*, 2013, **563**, 293–299.

22 J. Choi, J. C. Kim, Y. B. Lee, I. S. Kim, Y. K. Park and N. H. Hur, Fabrication of silica-coated magnetic nanoparticles with highly photoluminescent lanthanide probes, *Chem. Commun.*, 2007, 1644–1646.

23 D. G. Papageorgiou, I. A. Kinloch and R. J. Young, Mechanical properties of graphene and graphene-based nanocomposites, *Prog. Mater. Sci.*, 2017, **90**, 75–127.

24 O. P. Kumar, M. N. Ashiq, M. Ahmad, S. Anjum and A. Ur Rehman, Silver and yttrium-doped bismuth vanadate for photoluminescent activity and boosted visible light-induced photodegradation, *J. Mater. Sci. Mater. Electron.*, 2020, **31**, 21082–21096.

25 S. Aime, S. G. Crich, E. Gianolio, G. B. Giovenzana, L. Tei and E. Terreno, High sensitivity lanthanide(III) based probes for MR-medical imaging, *Coord. Chem. Rev.*, 2006, **250**, 1562–1579.

26 P. Macaudie, Low-temperature process of the cubic lanthanide sesquisulfides: remarkable stabilization of the c-Ce S phase, *J. Mater. Chem.*, 1997, **7**, 1541–1547.

27 V. J. Mane, S. B. Kale, S. B. Ubale, V. C. Lokhande, U. M. Patil and C. D. Lokhande, Lanthanum sulfide-manganese sulfide/graphene oxide (La$_2$S$_3$-MnS/GO) composite thin film as an electrocatalyst for oxygen evolution reactions, *J. Solid State Electrochem.*, 2021, **25**, 1775–1788.

28 J. Wu, K. Fujii, M. Yashima, A. Staykov, T. Akbay, T. Ishihara and J. A. Kilner, A systematic evaluation of the role of lanthanide elements in functional complex oxides; implications for energy conversion devices, *J. Mater. Chem. A*, 2018, **6**, 11819–11829.

29 R. Chetty, S. R. Pandya and M. Singh, Physicochemical interaction of cerium oxide nanoparticles with simulated biofluids, hemoglobin, insulin, and ds-DNA at 310.15 K, *New J. Chem.*, 2020, **44**, 1825–1845.

30 J. Yin, Y. Hu and J. Yoon, Fluorescent probes and bioimaging: Alkali metals, alkaline earth metals and pH, *Chem. Soc. Rev.*, 2015, **44**, 4619–4644.

31 D. Kumar, A. Chandra and M. Singh, Influence of Urea on Shifting Hydrophilic to Hydrophobic Interactions of Pr(NO$_3$)$_3$, Sm(NO$_3$)$_3$, and Gd(NO$_3$)$_3$ with BSA in Aqueous Citric Acid: A Volumetric, Viscometric, and Surface Tension Study, *J. Chem. Eng. Data*, 2014, **59**(11), 3643–3651.

32 K. A. Gschneidner, Preparation and Processing of Rare Earth Chalcogenides, *J. Mater. Eng. Perform.*, 2000, **7**, 656–660.

33 Y. Han, Preparation of Calcium lanthanum Sulfide Powders *via* Alkoxide Su, *J. Am. Ceram. Soc.*, 1991, **19**, 2815–2819.

34 A. B. Ghosh, N. Saha, A. Sarkar, D. N. Srivastava, P. Paul and B. Adhikary, RSC Advances Solvent assisted and solvent free orientation of growth of nanoscaled lanthanide sulfides: tuning of morphology and manifestation of photocatalytic, *RSC Adv.*, 2015, **3**, 102818–102827.

35 X. Luo, M. Zhang, L. Ma and Y. Peng, Preparation and stabilization of γ-La2S3 at low temperature, *J. Rare Earths*, 2011, **29**, 313–316.

36 S. Rezania, A. Mojiri, J. Park, N. Nawrot, E. Wojciechowska, N. Marraiki and N. S. S. Zaghloul, Removal of lead ions from wastewater using lanthanum sulfide nanoparticle decorated over magnetic graphene oxide, *Environ. Res.*, 2022, **204**, 111959.

37 L. Li, S. Hirai and Y. Tasaki, Synthesis and sintering of samarium rich SmSx and its electrical property, *J. Rare Earths*, 2016, **34**, 1042–1047.

38 K. R. Kolte, K. Shah and B. S. Chakrabarty, Exploring lanthanum sulphide characteristics for its physical properties, *Int. J. Sci. Technol. Res.*, 2019, **8**, 957–961.

39 G. Avashthi and M. Singh, Ultrasound accelerated near-edge functionalized heterogeneous graphene oxide sonocatalyst for surface optical bandwidth efficacy and in situ sonothermocatalysis, *New J. Chem.*, 2021, **45**, 5463–5483.

40 S. Dev and M. Singh, Lanthanide sulfide decorated graphene oxide nanorods as an effective photocatalysts for reducing dyes, free radicals, and water split to produce H2 in sunlight, *Solid State Sci.*, 2022, **134**, 107045.

41 N. Vashistha, A. Chandra and M. Singh, HSA functionalized Gd$_2$O$_3$:Eu^{3+} nanoparticles as an MRI contrast agent and a potential luminescent probe for Fe^{3+}, Cr^{3+}, and Cu^{2+} detection in water, *New J. Chem.*, 2020, **44**, 14211–14227.

42 S. S. Maktedar, S. S. Mehetre, G. Avashthi and M. Singh, In situ sonochemical reduction and direct functionalization of graphene oxide: A robust approach with thermal and biomedical applications, *Ultrason. Sonochem.*, 2017, **34**, 67–77.

43 P. Aryanrad, H. R. Naderi, E. Kohan, M. R. Ganjali, M. Baghernejad and A. Shiralizadeh Dezfuli, Europium oxide nanorod-reduced graphene oxide nanocomposites towards supercapacitors, *RSC Adv.*, 2020, **10**, 17543–17551.

44 B. Hou, X. Wang, J. Wang, J. Yao, H. Zhang, W. Yu, G. Liu, X. Dong and L. Wang, In situ synthesis of homogeneous Ce$_2$S$_3$/MoS$_2$ composites and their electrochemical performance for lithium ion batteries, *RSC Adv.*, 2017, **7**, 6309–6314.

45 M. Singh and S. Singh, *Survismeter: Fundamentals, Concepts, and Applications*, Jenny Stanford Publishing, 1st edn, 2019, DOI: **10.1201/9780429027611**.

46 M. Singh, Survismeter-Type I and II for surface tension, viscosity measurements of liquids for academic, and research and development studies, *J. Biochem. Biophys. Methods*, 2006, **67**, 151–161.

47 M. Singh, Upper critical solution temperatures for immiscible solvent systems with halide salts, carboxylic acids, surfactants and polynuclear aromatic compounds and benzene derivatives, *J. Chem. Thermodyn.*, 2007, **39**, 240–246.

48 R. Mirzajani and S. Karimi, Ultrasonic assisted synthesis of magnetic Ni-Ag bimetallic nanoparticles supported on reduced graphene oxide for sonochemical simultaneous removal of sunset yellow and tartrazine dyes by response surface optimization: Application of derivative spectrophot, *Ultrason. Sonochem.*, 2019, **50**, 239–250.